Dual function of magnetic field in enhancing antibiotic wastewater treatment by an integrated photocatalysis and fluidized bed biofilm reactor (FBBR)

Yilin Dong [a], Jie Zhang [a], Qiuwen Wang [a], Dongyu Xu [a], Shaoxuan Pang [a], Luiza C. Campos [b], Zhijun Ren [a,*], Pengfei Wang [a,*]

a School of Energy and Environmental Engineering, Hebei University of Technology, Tianjin 300401, China

b Department of Civil, Environmental and Geomatic Engineering, University College London, London WC1E 6BT, United Kingdom

*Correspondence to: Z. J. Ren (E-mail: renzhijun2003@126.com) & P. F. Wang (E-mail: pengfeiwang@hebut.edu.cn)

Abstract

The integrated photocatalysis and fluidized bed biofilm reactor (FBBR) is an attractive wastewater treatment technique for managing wastewater containing antibiotics. However, the fast recombination of photoinduced charge and low microbial activity limit the degradation and mineralization efficiency for antibiotics. To address this, we attempt to introduce magnetic field (MF) to the integrated system with B-doped Bi_3O_4Cl as the photocatalysts to effectively improve removal and mineralization of ciprofloxacin (CIP). As a consequence, the degradation rate reaches 96% after 40 d in integrated system with MF. The biofilm inside the integrated system with MF carrier can mineralize the photocatalytic products, thereby increasing the total organic carbon (TOC) degradation rate by more than 32%. The electrochemical experiment indicates the Lorentz force generated by MF can accelerate charge separation, increasing the electron concentration. Simultaneously, the increased amounts of electrons lead to the generation of more $\cdot OH$ and $\cdot O_2^-$. MF addition also results in increased biomass, increased biological respiratory activity, microbial community evolution and accelerated microbial metabolism, enabling more members to biodegrade photocatalytic intermediates. Therefore, applied MF is an efficient method to enhance CIP degradation and mineralization by the integrated system.

Keywords: Photocatalysis, Biodegradation, Microbial metabolomics, Magnetic field, Lorentz force

1. Introduction

The water environmental concern has become one of the most crucial global challenges with the continuous development of industrialization and urbanization facing the world today (Sousa et al., 2018; Zhang et al., 2016). The integrated photocatalysis and fluidized bed biofilm reactor (FBBR) technique presents potential applications in improving the degradation and mineralization of recalcitrant compounds (Zhou et al., 2015; Ma et al., 2018; Fu et al., 2021; Ding et al., 2018). In an integrated photocatalysis and FBBR system, macroporous carriers support photocatalysts on their exterior surface and biofilm development on their inside. In this case, the photocatalytic reactive oxygen species (ROSs) attack recalcitrant compounds on the outer surface of carriers, producing biodegradable intermediates that can be instantly used by the internal microorganisms for further mineralization (Zhao et al., 2018; Dong et al., 2023). Nevertheless, the photocatalysis process is mainly confined by the recombination speed of photogenerated carriers. Simultaneously, biofilms are vulnerable to the toxicity of pollutants and are also affected by free radicals and light, resulting in slow growth and low activity. This results in low efficiency in the treatment of pollutants by integrating photocatalysis with FBBR. Therefore, it is necessary to improve the photocatalytic performance and promote biological growth simultaneously.

Recently, the MF-enhanced photocatalytic activity has received extensive attention. In the domain of photocatalysis, there are many reports on the magnetic field (MF) enhancement, since it does not alter the geometries or compositions of the

23 photocatalysts and there is no need for complex preparation processes. MF is a fairly

24 simple, practical, non-contact, and environment-friendly method that can be realized

25 just by placing permanent magnets (Li et al., 2018). MF can expedite the separation

26 and transfer of photoinduced carriers by the Lorentz force (Anwer et al., 2022). The

27 Lorentz force in a MF, the force generated on a charge caused by the relative motion

28 between the charge and the MF, is defined as: $\vec{F}=q\,(\vec{V}\times\vec{B})$, where q is the particle

29 charge and $\vec{V}$ is the velocity of a particle moving in a MF with a magnetic induction

30 intensity $(\vec{B})$. According to the left-hand rule, a moving charge in a MF should

31 undergo a force perpendicular to the direction of the MF plane motion, which causes a

32 deviation of the charge motion (Gao et al., 2019). Consequently, the electron and hole

33 experience opposite forces because of their opposite charges and diverge in opposite

34 directions, thus accelerating the separation and transfer of photoinduced electron and

35 hole (Gao et al., 2019). Meanwhile, MF effects is a technique developed in recent

36 years to enhance the growth rate and activity of microorganisms. As a physical factor,

37 MFs cannot touch off the generation of chemical secondary contaminants.

38 Furthermore, MF intensity can be precisely and easily commanded, allowing for

39 extensive applications (Yan et al., 2022). MF applications are promising, including

40 protein recovery, cell filtration, enzyme immobilization, fermentation, affinity

41 chromatography, microbial, plant cell culture treatment and biological wastewater

42 treatment processes (Yavuz et al., 2000). According to previous researches, MFs may

43 affect microbial gene expression, enzyme reaction activity, free radical production,

44 and cell membrane characteristics (Albuquerque et al., 2016). In addition, by affecting

45   the metal ions of the active center site to alter the conformation, so as to enhance the

46   enzyme activity (Strašák et al., 2002). Inspired by this, MF cannot only speed up the

47   separation and transfer of photoinduced charge, but also accelerate growth rate and

48   activity of microorganisms, thus synergistically enhancing the removal of pollutants.

49   However, there is no report on the application of MF to integrated photocatalysis and

50   FBBR system to synergistically enhance the pollutants degradation by speeding up

51   separation and transfer of photoinduced charges and promoting microbial growth and

52   activity, and the potential mechanism is still largely unclear.

53   Therefore, the aim of this study was to investigate for the first time, the application

54   of MF in integrated photocatalysis and FBBR system. The strengthening mechanism

55   of ciprofloxacin (CIP) removal and mineralization was assessed in a

56   visible-light-induced integrated photocatalysis and FBBR process with B-Bi$_3$O$_4$Cl

57   (B-BOC) as the photocatalyst by MF. The photo-electrochemical measurements, SEM

58   and gene function were implemented to study impacts of the photogenerated charges

59   and microbial activity on MF. Furthermore, chemical oxygen demand (COD), total

60   organic carbon (TOC), microbial response, and CIP degradation pathways were

61   analyzed. The microbial community and metabolism changes in integrated

62   photocatalysis and FBBR system were also examined.

63   **2. Materials and methods**

64   *2.1. The integrated photocatalysis and FBBR system fabrication*

65   *2.1.1. Photocatalysts coating*

66   The porous carrier of this study was 10 mm x 10 mm x 10 mm with aperture of 300

67 ~ 800 μm of polyurethane, porosity of 98% (Fig. S1). In this study, effective and

68 low-cost B-BOC nanosheets were used as photocatalysts. The B-BOC was

69 synthesized by a hydrothermal method (Dong et al., 2021). The detailed preparation

70 and characterizations of B-BOC are shown in Text S1 and Figs. S2-5. The coating

71 was performed by ultrasonically dispersing 2.0 g B-BOC into 20 mL of ethanol and

72 diffusing 2 mL of HNO_3 into the solution. Then, the above solution was heated to 80 °C

73 for 30 min. And the carriers with a volume ratio of 1:1 (V/V) were mixed in the

74 suspension through ultrasound for 30 min. The carriers absorbed the photocatalysts

75 and were dried at 60 °C. The obtained coating carrier is defined as sponge@B-BOC

76 (Fig. S6).

77 *2.1.2. Biofilm cultivation*

78 The activated sludge was obtained from aerobic sludge of a sewage treatment plant.

79 The photocatalyst-coated carriers were cultured in a fluidized bed reactor driven by

80 internal circulation airlift. The synthesized feedwater contained (mg/L) 432 $C_6H_{12}O_6$,

81 137 peptone, 10 $(NH_4)_2SO_4$, 50 KH_2PO_4, 50 $Na_2HPO_4 \cdot 2H_2O$, 50 $MgSO_4$, 5

82 $CaSO_4 \cdot 2H_2O$ and 10 $FeCl_3$. During microbial domestication, 40.0 mg/L ciprofloxacin

83 (CIP) was added for about two months. After microbial acclimatization and

84 stabilization, the sponge@B-BOC were mixed in the activated sludge reactor for 10

85 days for microbial colonization. Finally, the growing biofilm sponge@B-BOC was

86 received, which was recorded as sponge@B-BOC@biofilm.

87 *2.2. Experimental setup and protocols*

88 CIP degradation was conducted in an internal circulation airlift-driven fluidized bed

89 reactor with a working volume of 800 mL (Fig. S7). Its configuration details are

90 displayed in Text S2. Air was supplied by a 35 W aeration pump. Illumination was

91 provided by an external LED panel (42 W), giving light with wavelength of 420-800

92 nm (visible light). Magnetic rods were placed on both sides outside the reactor to

93 generate a static MF.

94 The two series were named integrated system-1 and integrated system-2 for

95 non-MF (NMF) and MF, respectively. During integrated system, both photocatalysis

96 and biodegradation occurred on the sponge carriers (described below). The same

97 integrated system also was run by sponge@B-BOC; these strictly photocatalytic tests

98 were defined as PC-1 and PC-2 for with NMF or MF, respectively. Again, the reactor

99 was run by sponge@B-BOC@biofilm, but in the dark; these biodegradation-only tests

100 were defined as FBBR-1 and FBBR-2 for with NMF or MF, respectively.

101 *2.3. Analysis of CIP and intermediates Analytical methods*

102 The CIP concentration was measured by an Agilent 1100 high-performance liquid

103 chromatography (HPLC) system with a 4.6×250 mm, 5 μm Athena HILIC C18

104 column. The wavelength of the ultraviolet (UV) detector was set at 278 nm. The

105 mobile phase (v/v) is 80% water/formic acid (9/1, V: V) and 20% methanol at a flow

106 rate of 1.0 mL/min.

107 CIP-photocatalysis products were tested using an ultra-performance liquid

108 chromatography tandem mass spectrometry (UPLC-MS) system by an ACQUITY

109 UPLC BEH C18 column (1.7 μm, 100×2.1 mm). The mobile phase was a mixture of

110 67% phosphoric acid aqueous solution (0.5%) and 33% methanol, which was applied

111 at a flow rate of 0.25 mL/min.

112 *2.4. DNA extraction and microbial community analysis*

113 During the selection period, biological samples were taken from original sludge,

114 form the integrated system-1 at days 20 and 40, and from the integrated system-2 at

115 days 17 and 40. The DNA of biological samples was extracted by a E.Z.N.A.® soil

116 DNA kit (Omega Bio-tek, Norcross, GA, U.S.). The DNA concentration was

117 determined using NanoDrop 2000 UV-vis spectrophotometer (Thermo Scientific,

118 Wilmington, USA). 338F (ACTCCTACGGGAGGCAGCAG) and 806R

119 (GGACTACHVGGGTWTCTAAT) primers were selected to amplify the bacterial

120 16S rRNA V3-V4.

121 *2.5. Metagenome sequence, assembly, gene prediction, and annotations*

122 DNA was extracted from each sludge using Covaris M220 (Gene Company

123 Limited, China) and fragmented to an average size of about 400 bp for the

124 construction of paired-end library. Paired-end sequencing was conducted on an

125 Illumina Hiseq Xten platform (Illumina Inc., San Diego, CA, USA) at Majorbio

126 (Shanghai, China). Data cleaning was carried out by trimming low-quality reads (< 50

127 bp) using fastp v 0.20.0.

128 Based on the concise de Bruijn graph way, MEGAHIT v 1.1.2 was used to

129 assemble the clean reads. Then MetaGene was used to predict combination contigs (≥

130 300 bp). Redundant genes were removed, and CD-HIT was used to cluster

131 non-redundant gene catalogue with 90% recognition rate and 90% coverage. Genes

132 were also annotated by comparing unigenes with those in functional databases, such

133 as Kyoto Encyclopedia of Genes and Genomes (KEGG) and CAZy.

3. Results and discussion

3.1. Improving CIP degradation and mineralisation using MF

To investigate the effect of MF on photocatalysis, we analysed the photocatalytic degradation performances when using sponge@B-BOC under varying MF intensities. As depicted in Fig. 1a, the CIP removal rate in the PC process exhibited a progressive increase under identical reaction conditions with increasing MF intensity, indicating that MF positively affected the photocatalytic activity. Furthermore, we conducted a detailed examination of the relation between MF intensity and the efficiency of photomagnetic coupling degradation of CIP. The obtained data was subjected to plotting and curve fitting, resulting in Fig. 1b. Notably, the fitting of the removal rate as a function of external MF intensity conformed to a quasi-first-order dynamic model (Fig. 1b), with an R^2 value of 0.9696. This high R^2 value signifies a strong correlation between the two parameters, implying that the removal rate increases linearly with increasing MF intensity.

To gain further insight into the role of MF in the integrated system, we assessed the efficiencies of CIP and COD removal in the presence of sponge@B-BOC@biofilm under varying MF intensities. As illustrated in Fig. 1c, the mean CIP degradation efficiencies for integrated system-2 under five MF intensities were 59.5%, 67.11%, 74.07%, 87.95% and 87.2%. Corresponding efficiencies for integrated system-1 were 55.35%, 60.93%, 67.52%, 76.74% and 80.44%. Notably, integrated system-2 consistently exhibited significantly higher CIP degradation efficiencies than integrated

155 system-1 at each stage. Furthermore, the CIP removal rate of integrated system-2

156 increased with increasing MF intensity, reaching a peak of 92.88% at 40 mT, after

157 which it slightly decreased with increasing MF intensity. Notably, the initial state of

158 integrated system-2 at 10 mT was affected by MF, resulting in temporary inhibition of

159 microbial activity in a more complex environment compared with integrated system-1.

160 This result can be attributed to the cumulative effect of MF on microorganisms, owing

161 to which a certain duration is required for the manifestation of enhanced effects

162 (observed from 20 to 50 mT). Over time, microbial activity improved and the external

163 MF caused the moving charged particles to be subjected to the Lorentz force,

164 ultimately enhancing the CIP removal rate. Furthermore, the trend of COD

165 degradation in both integrated system-1 and integrated system-2 was similar to that of

166 CIP (Fig. 1d). Consequently, integrated system-2 exhibited faster adaptation to the

167 CIP environment, achieving higher CIP and COD removal efficiencies. Additionally,

168 Fig. S8 illustrates the variation in dehydrogenase activity (DHA) as MF intensity in

169 integrated system-1 and integrated system-2, affirming that weak MF exerts a positive

170 catalytic effect on enzyme activity. Therefore, we selected 40 mT as the optimum

171 magnetic induction intensity for subsequent tests.

172 For the short-term tests conducted for 12 h, the various results for each system are

173 presented in Fig. 1e. In case of single biodegradation reactions, the presence of

174 biofilm led to a CIP adsorption rate of only 35.9% for FBBR-1 after 12 h. However,

175 the CIP adsorption rate for FBBR-2 did not considerably improve under the influence

176 of MF. Although magnetic induction intensity can promote microbial activity in

177 activated sludge, all organisms can detach owing to the toxic effects of strongly

178 inhibitory CIP. Consequently, the adsorption of CIP for both FBBR-1 and FBBR-2

179 tends to be similar. The CIP removal rate for photocatalysis alone was considerably

180 higher under MF than under NMF conditions. This result suggests that the Lorentz

181 force generated by MF effectively restrains the recombination of photoinduced

182 carriers, ultimately accelerating the CIP degradation rate in PC-2. The degradation

183 effect of integrated system-1 on CIP gradually improved and eventually stabilised.

184 Notably, the CIP degradation rate in integrated system-2 was substantially higher than

185 in integrated system-1 under MF.

186 The degradation kinetics of CIP in PC-1, PC-2, integrated system-1 and integrated

187 system-2 were fitted using quasi-first-order kinetics. The change in reaction rate

188 constant (k) provides a better understanding of the CIP degradation efficiency in these

189 systems. Fig. 1f and Table S1 show that the k value for CIP removal in PC-1 is 0.05

190 h^{-1}, while that for CIP degradation in integrated system-1 is 0.098 h^{-1}. This difference

191 highlights the higher CIP removal rate in integrated system-1, likely attributed to the

192 utilisation of intermediate compounds by the microorganisms in this integrated system.

193 In case of PC-2, under the influence of MF, the k value for CIP degradation is 0.099

194 h^{-1}, indicating that MF has a certain effect on the photocatalytic removal of CIP.

195 Moreover, the CIP degradation efficiency in integrated system-2 shows improvement.

196 A similar trend is observed in UV–vis spectrums related to CIP removal (Fig. S9).

197 This enhancement may be attributed to the effective restraining of photogenerated

198 carrier recombination under the influence of magnetic Lorentz force, which enhances

199   the photocatalytic CIP removal rate on the carrier surface. Additionally, a specific

200   magnetic induction intensity can promote microbial and oxidase activity in the

201   activated sludge, further enhancing the CIP removal rate.

202   In PC-1, the mineralisation rate of CIP within 12 h is only 44%. This indicates that

203   without external MF, the photocatalytic oxidation process exhibits poor efficiency in

204   terms of CIP mineralisation. However, the CIP mineralisation efficiency improves in

205   PC-2 under MF. Upon coupling biodegradation, integrated system-1 shows a

206   considerable improvement in TOC removal efficiency, with an increase of 22.92%

207   compared with PC-1 (Fig. 1g). This confirms the crucial role of microorganisms in

208   CIP mineralization in integrated system-1. Furthermore, the TOC degradation

209   efficiency in integrated system-2 is further enhanced under MF. Compared with

210   integrated system-1, the TOC removal rate in integrated system-2 is increased by 23%,

211   indicating that MF can improve TOC removal efficiency in the integrated system.

212   This conclusion is corroborated by the findings presented in Fig. S10.

213   To assess the stability of integrated system-2 in degrading CIP and COD, we

214   conducted a 40-day experiment involving successive FBBR, PC, and integrated

215   system under the influence of MF, as depicted in Figs: 2a and 2b. Fig. 2c provides an

216   overview of the experimental setup. In case of single biodegradation reactions, the

217   CIP adsorption rate of CIP for FBBR-1 was only ~30% after stable operation, while

218   that for FBBR-2 barely improved. This phenomenon can be attributed to the fact that

219   although magnetic induction increased the activity of microorganisms in the activated

220   sludge, these microorganisms detached owing to the toxic effects of strongly

221   inhibitory CIP. Consequently, we observed consistent CIP adsorption for FBBR

222   regardless of the presence of MF. A similar trend was observed in the COD

223   degradation process. In the PC-2 system, a notable improvement in CIP degradation

224   performance was observed, possibly owing to the Lorentz force generated by MF,

225   which effectively accelerated charge separation, increased the number of electrons

226   participating in the photocatalytic process and ultimately improved the efficiency of

227   CIP degradation. This suggests that MF effectively enhances the photocatalytic

228   degradation rate of high-concentration CIP. Fig. 2b shows that the COD degradation

229   efficiency in PC-1 gradually decreased owing to the initial adsorption of CIP by the

230   sponge carrier, indicating that photocatalysis has a limited effect on CIP

231   mineralisation. Conversely, in PC-2, the COD removal rate slightly improved,

232   indicating that MF can enhance COD removal efficiency. Unlike FBBR and PC, the

233   biofilm loads on the external surface of the carriers in the integrated system were

234   rapidly shed in the early stages of the reaction regardless of the presence of MF owing

235   to the erratic nature of the reaction, resulting in fluctuating CIP degradation rates.

236   However, as the reaction progressed, the CIP removal rate stabilised, possibly because

237   the biofilm on the exterior of the carriers fell off, exposing the photocatalysts and

238   forming an effective integrated system. Under the optimal magnetic induction

239   intensity, the CIP removal rate was 18.78% higher than that of integrated system-1.

240   Fig. 2b shows that the COD removal rate in integrated system-2 was 23.73% higher

241   than in the absence of MF. The application of MF and a specific magnetic induction

242   intensity promoted microbial and oxidase activity, improved microbial membrane

243 permeability and effectively inhibited photogenerated carrier recombination under the

244 influence of the Lorentz force. This led to an enhancement in electron concentration,

245 thereby improving the COD removal efficiency. In summary, MF helps the integrated

246 system to enhance the CIP and COD removal rates. Moreover, MF enables integrated

247 system-2 to maintain stable removal efficiency and adapt to challenging

248 environmental conditions. Additionally, the loading amount of B-BOC on the carriers

249 exhibited only a mild decrease after 40 days, indicating enduring adhesion strength

250 (Fig. S11).

251   An ESR diagram was employed to assess the presence of free radical intermediates

252 in both the PC and integrated systems. As shown in Fig. 2d, the $\cdot OH$ signal, captured

253 by DMPO, is detected for both the PC and integrated systems. However, when

254 comparing the PC system to the integrated system, only a slight change in the spectral

255 strength of $\cdot OH$ is observed for the integrated system. Fig. 2e displays ESR signals for

256 DMPO-$\cdot O_2^-$ in both the PC and integrated systems, with the ESR signal being

257 substantially stronger for the integrated system. This enhancement in the $\cdot O_2^-$

258 spectrum may be attributed to additional photoelectron transfer between B-BOC and

259 the biofilm in the integrated system. The signal intensity of $\cdot OH$ and $\cdot O_2^-$ in B-BOC

260 and B-BOC@biofilm is considerably enhanced under MF. This supports the notion

261 that the Lorentz force generated by MF effectively accelerates charge transfer

262 capabilities, increases electron population, and consequently generates more free

263 radicals. Therefore, MF can enhance the generation of free radicals. Furthermore, the

264 results from the ESR analysis indicate that $\cdot OH$ and $\cdot O_2^-$ are the primary free radicals

265 present in integrated system-2.

266 *3.2. Impact of MF on photo-electrochemical measurements and oxygen transfer*

267 A series of measurements were performed to further study the causes for the

268 increase in $\cdot OH$ and $\cdot O_2^-$ generation under MF. First, photocurrent response tests were

269 conducted to account for the motion of charged particles experiencing the Lorentz

270 force in MF. As shown in Fig. 3a, B-BOC-1 rapidly generates photocurrent under

271 visible light irradiation (Fig. 3a), indicating a high rate of photoelectron transmission.

272 Moreover, when a biofilm covers the electrode, there is a mild increase in

273 photocurrent owing to photoelectron transfer between B-BOC-1 and the biofilm. The

274 photocurrent intensity under MF is considerably higher than that under NMF

275 conditions, indicating that the Lorentz force generated in MF effectively accelerates

276 photogenerated charge separation and transfer.

277 Electrochemical impedance spectroscopy (EIS) provides valuable insights into the

278 separation efficiency and transfer resistance of photoinduced carriers. Fig. 3b shows

279 that the semicircle size of integrated system-1 is smaller than that of PC-1. This

280 implies that integrated system-1 can generate more electrons for transfer than PC-1,

281 confirming the existence of photoelectron transfer between B-BOC-1 and

282 microorganisms. Furthermore, the EIS Nernst curves of the B-BOC-2 and

283 B-BOC@biofilm-2 samples under MF are smaller than those under NMF conditions.

284 This result indicates the transfer resistance is reduced under MF, highlighting the

285 effectiveness of the Lorentz force generated under MF in inhibiting photogenerated

286 carrier recombination. Furthermore, when light is combined with MF, the slopes of

287 the Mott–Schottky plot are further reduced, indicating a higher charge carrier

288 concentration generated by MF (Fig. 3c). In summary, the enhancement in

289 photocatalytic activity can be primarily attributed to the increased quantity of

290 separated photogenerated carriers under MF.

291   Furthermore, time-dependent open-circuit potential decays (OCPDs) were

292 conducted under two conditions: NMF and MF. When B-BOC nanosheets were

293 exposed to light, a distinct open-circuit potential (OCP) response was observed, both

294 in the presence and absence of the MF (Fig. 3d). Moreover, an increase of 0.133 V in

295 the open-circuit voltage was observed under MF was compared with the open-circuit

296 voltage obtained under the NMF condition. This increase indicates that the Lorentz

297 force generated by MF enhances the separation of photogenerated carriers in the

298 B-BOC-2 nanosheets. Furthermore, when both the biofilm and photocatalyst were

299 present simultaneously, an enhancement in OCP was observed. In particular, the

300 OCPD rate of B-BOC@biofilm-1 in integrated system-1 was slower than that in the

301 PC-1 system, suggesting delayed recombination kinetics of charges. Moreover,

302 B-BOC@biofilm-1 exhibited a prolonged electron lifetime, implying that many

303 electrons were involved in the reaction in integrated system-1. This observation

304 confirms photoelectron transfer between the photocatalyst and biofilm (Fig. S12).

305 Furthermore, the electron transfer rate was accelerated under the influence of the MF,

306 thereby demonstrating the enhancement of photocatalytic efficiency by MF. Fig. 3e

307 illustrates the diagrammatic representation of the transfer mechanism of the

308 photogenerated charge carriers under MF conditions. The Lorentz force acts on the

photogenerated electrons and holes, compelling them to move in opposite directions

as they traverse the liquid stream and intersect the magnetic induction lines, thereby

accelerating the separation and transfer of charges. When additional MF is applied,

the Lorentz force acts in the opposite direction on the photoinduced electrons and

holes, promoting their spatial separation and transport. This leads to an increase in the

number of electrons participating in the photocatalytic process.

Furthermore, the application of the MF also disrupts hydrogen bonds, leading to the

elongation of conjugated water molecules, which are subsequently truncated into

shorter conjugated forms. This transformation increases water activity and oxygen

transfer rate. Oxygen transfer is a complex mass transfer phenomenon occurring

between the gas and liquid phases. Therefore, the volumetric gas–liquid mass transfer

coefficient ($k_L a$) can be used to investigate the oxygen transfer rate. As depicted in Fig.

S13a, the equilibrium concentrations of dissolved oxygen in water under NMF and

MF conditions were 6.92 and 7.01 $mg \cdot L^{-1}$, respectively. Fig. S13b shows that the

calculated $k_L a$ values were 0.00534 and 0.00812 s^{-1} under NMF and MF conditions,

respectively. Notably, the introduction of MF led to a considerable increase in $k_L a$ by

approximately 52.06% compared with the MF condition. These findings affirm that

introducing MF effectively enhances the volumetric gas–liquid mass transfer

coefficient, consequently improving the oxygen transfer rate in water. Such

improvements are highly beneficial for the overall efficiency of photocatalytic

reactions.

3.3. Enhanced microbial survival and activity

331   Maintaining rich biomass and ensuring high biological activity in the carrier are

332   critical factors influencing the degradation efficiency and mineralisation degree of

333   CIP when treated by the integrated system. To analyse the effect of MF on the

334   microorganisms of the integrated system, we conducted observations of the biofilm

335   present on the carrier using scanning electron microscopy (SEM). Figs. 4a and b show

336   that the interior and exterior surfaces of the carrier are densely covered with a biofilm

337   that adheres to its skeleton. After the integrated reaction, an ideally coupled composite

338   carrier is formed, regardless of the presence of the MF. This transformation

339   completely detaches the biofilm from the carrier surface, exposing most

340   photocatalysts (as depicted in Figs. 4c and e). Simultaneously, the biofilm in the inner

341   channels of the carrier remains protected, as illustrated in Figs. 4d and f.

342   Nonetheless, we observed that MF exerts a particular influence on the biofilm

343   inside the carrier. In terms of biomass, the biofilm inside the carrier before the

344   reaction exhibits relatively high density and substantial biomass, as shown in Fig. 4a.

345   However, in case of integrated system-1, although the biofilm inside the carrier is

346   relatively dense, its biomass undergoes considerable reduction, as illustrated in Fig.

347   4d. Moreover, the biofilm inside the carrier is also dense and its biomass surpasses

348   that of integrated system-1 under MF conditions, as depicted in Fig. 4f. This

349   observation suggests that MF effectively promotes biofilm growth within the carrier.

350   Furthermore, we conducted confocal laser scanning microscopy (CLSM) to

351   examine the survival of microorganisms on the carrier closely. Initially, after

352   membrane culture, the biofilm on the carrier displayed a remarkable ratio of 91% live

353 bacteria to 9% dead bacteria, indicating the organisms maintain high activity (refer to

354 Fig. 5a). However, following a distinct biodegradation reaction, the ratio of live

355 bacteria to dead bacteria within the biofilm on the carrier in FBBR-2 shifted

356 drastically to 16% live and 84% dead, underscoring the potent bactericidal effect of

357 CIP on the biofilm. In contrast, in integrated system-1, the proportion of living

358 bacteria within the biofilm on the carrier during CIP degradation after the integrated

359 reaction decreased to only 67%, with 33% of cells succumbing to the inhibitory

360 effects of CIP on the biofilm. Moreover, in integrated system-2 under the influence of

361 the MF, the ratio of live bacteria to dead bacteria within the biofilm on the carrier

362 stood at 86% live and 14% dead, essentially maintaining the levels observed after

363 membrane culture. This signifies a 19% increase in the proportion of living bacteria

364 under MF compared to integrated system-1. It further corroborates that while CIP

365 inhibits the biofilm in integrated system-2, the MF enhances the cellular membrane

366 activity, consistent with the SEM observations.

367   The effect of the MF on the biodegradation in the integrated system is twofold.

368 First, this effect is evident in improving biofilm biomass and biological activity.

369 Second, MF promotes the succession of the biofilm community structure in the carrier.

370 Figs. 5b and S14 illustrate the changes in the biofilm community structure on the

371 carrier before and after integrated system-1 and integrated system-2. After initial

372 cultivation with activated sludge as the inoculation source (referred to as 'Initial'), the

373 dominant genera in the biofilm community structure on the carrier are *Zoogloea*

374 (13.15%), *Acinetobacter* (17.52%), *Acidororax* (7.24%), *Lactobacillus* (23.52%),

375 *Clostridium_sensu_stricto_1* (7.74%) and *Pseudomonas* (6.36%). These genera are

376 typical of activated sludge bacteria (Zhang et al., 2011). Among these genera,

377 *Pseudomonas* is an obligate aerobic gram-negative non-spore-forming bacillus, a

378 prominent bacterium in activated sludge communities. During the process of CIP

379 degradation, there is a considerable decrease in the relative abundance of

380 *Acinetobacter* and *Acidororax*. This decline suggests that these bacteria are not

381 well-suited to the challenging environment created by CIP and are gradually

382 eliminated. Conversely, *Pseudoxanthomonas* and *Sphingomonas* exhibit enrichment

383 in both integrated system-1 and integrated system-2 during the reaction. Notably,

384 *Pseudoxanthomonas* has been verified to contain CIP resistance genes. At the same

385 time, *Sphingomonas* possesses a notable capacity for degrading aromatic hydrocarbon

386 pollutants in sewage (Albert et al., 2000). These findings highlight the importance of

387 the biofilm in an integrated system. Accordingly, the biofilm can further mineralise

388 the intermediate products generated through CIP photocatalysis. Consequently, the

389 biofilm plays a pivotal role in the mineralisation and degradation of CIP.

390   However, the community structure of the biofilm in integrated system-2 clearly

391 differs from that in integrated system-1 under the influence of MF. Initially, the

392 relative abundance of *Ferruginibacter* in the biofilm sample was 0.32% before the

393 integrated reaction. Subsequently, after the integrated photocatalysis and FBBR

394 system reactions, it experiences considerable enrichment in integrated system-1 and

395 system-2. However, its relative abundance in integrated system-2 surpasses that in

396 integrated system-1. This suggests that *Ferruginibacter* exhibits a robust adaptability

to MF, and the presence of MF promotes its growth. *Pseudomonas*, an aerobic

heterotrophic microorganism able to utilise a wide range of organic substances,

including complex organic compounds resistant to degradation by other organisms,

also exhibits a higher biomass under enhanced MF conditions compared to integrated

system-1. Furthermore, the abundance of *Lysinibacillus*, *Clostridium*, *Bacillus* and

Comamonas in integrated system-2 exceeds that in integrated system-1. Among these,

Clostridium is known for its effective cleavage of aromatic rings (Wojcieszynska et al.,

2011). Previous studies have indicated that *Lysinibacillus* and *Bacillus* possess

inherent resistance to CIP (Olivares et al., 2013). Comamonas has also been reported

to be able to degrade aromatic compounds and their derivatives (Wojcieszynska et al.,

2011). Therefore, *Lysinibacillus*, *Clostridium*, *Bacillus* and *Comamonas* contribute to

the degradation of metabolites and adapt well to the MF environment. Moreover,

Lysinibacillus, *Pseudomonas*, *Burkholderia* and *Bacillus*, known for their

extracellular electron transfer ability, exhibit significant increases under MF

conditions (Nandy et al., 2013). This indicates that MF effectively promotes the

transfer of photoelectrons between microorganisms and photocatalysts. Microbes can

use these photoelectrons' energy to re-establish their microbial communities. At the

phylum level, Proteobacteria dominates all reactors by the end of the enrichment stage,

with relative abundances ranging from 45.77% to 57.8%. Interestingly, the abundance

of proteobacteria under MF conditions is 1.36-fold higher than that under NMF

conditions, signifying a positive impact of MF. In summary, MF proves beneficial in

adjusting and optimising the structure of the dominant bacterial community, thereby

419   maintaining the species abundance within the reactor.

420   Furthermore, a comparison between the biological samples from integrated

421   system40-2 and the initially activated sludge reveals significant differences, as

422   demonstrated in the Venn diagram (Fig. 5c). Among the 569 ASVs shared by five

423   biological samples, 67 ASVs are unique to the cultivated sludge, and no ASVs are

424   detected in the other four biological samples following the reactions, whether with or

425   without MF. Interestingly, the number of unique ASVs in integrated system40-2 and

426   integrated system17-2 is notably high, reaching 403 and 356, respectively. These

427   findings are consistent with the results obtained from the principal component

428   analysis (PCA) (Fig. S15) and the mean proportions of microbial samples (Fig. S16).

429   These observations collectively indicate that MF induces changes in the richness of

430   the microbial community, which proves advantageous for stabilising and enhancing

431   biofilm activity. Moreover, the increase in Chao1, ACE, and Shannon diversity

432   indexes and a reduction in the Simpson diversity index in integrated system-2

433   suggests that MF contributes to heightened microbial community abundance and

434   diversity (see Table S2).

435   To provide a more direct comparison of biofilm activity between integrated

436   system-1 and integrated system-2, we measured dehydrogenase activity (DHA) during

437   the reaction process (Fig. 5d). Before the reaction, the activity of the unit mass of

438   biofilm is measured at 0.366 mg TF. However, DHA decreases after the integrated

439   system reaction. Notably, MF significantly elevates biofilm activity in integrated

440   system-2 compared to integrated system-1, indicating that MF can enhance biofilm

441 activity. In addition to DHA, the activation of the electron transfer system (ETS) is

442 another crucial indicator for evaluating microbial activity. ETS activation reflects the

443 degree of inhibition in the electron transfer process during microbial respiration.

444 When assessing the overall performance of microbial respiration in the presence of 40

445 mg/L CIP under NMF conditions (Fig. 5e), it becomes evident that CIP initially

446 inhibits microbial respiration and reaches its maximum inhibitory effect on the 5th day.

447 ETS activation decreases from 288.45 mg/(g·h) to 218.4 mg/(g·h). Subsequently, ETS

448 activation stabilises and gradually recovers to the observed level before adding CIP,

449 suggesting that the impact of 40 mg/L CIP on microbial respiration dissipates after 25

450 days. In contrast, with the application of MF, CIP initially inhibits microbial

451 respiration and reaches its maximum inhibitory effect by the 10th day. ETS activation

452 decreases from 289.4 mg/(g·h) to 226.85 mg/(g·h). Subsequently, ETS activation

453 stabilises and gradually returns to the level observed before CIP was introduced,

454 indicating that the effect of CIP on microbial respiration disappears after 30 days.

455 These results suggest that ETS activation decreases briefly upon introducing CIP and

456 returns to normal levels. The critical difference is that under MF, CIP fully

457 demonstrates its effect on ETS activation by the 10th day, while under NMF, it takes

458 until the 5th day. This implies that MF can promote microbial respiration.

459 *3.4. MF effect on gene function and metabolic pathways*

460 To investigate the metabolic differences between the NMF and MF processes, we

461 employed metagenomic analysis to quantify the activity of metabolic pathways.

462 Triplicate biological samples were collected from the integrated system-1 and

463　integrated system-2 reactors on the 40th day. These samples were subsequently

464　thoroughly mixed to ensure uniformity for DNA extraction.

465　　The carbohydrate-active enzymes (CAZy) database encompasses enzymes involved

466　in synthesising, metabolising and modifying carbohydrates. These enzymes are

467　categorised into six functional groups: (1) glycoside hydrolases (GHs); (2) glycosyl

468　transferases (GTs); (3) polysaccharide lyases (PLs); (4) carbohydrate esterases (CEs);

469　(5) ancillary activities (AAs); and (6) carbohydrate-binding modules (CBMs)

470　(Cantarel et al., 2009). In integrated ssyetm40-2, the proportions of these groups are

471　as follows: PLs (0.8%), AAs (11.2%), CEs (20.9%), GHs (36.7%), GTs (29.1%) and

472　CBMs (1.3%) (Fig. 6a). Notably, the percentages of GHs and CEs are higher than

473　those in integrated system40-1. The GH family encompasses various hydrolases, such

474　as cellulases, cellobiohydrolases, endo-/exo-glucanases and arabinofuranosidases

475　(Gullert et al., 2016). On the other hand, the GT family is responsible for catalysing

476　glycosylation reactions involving NDP-sugars and glycosinosides (Cantarel et al.,

477　2009). Hence, it can be inferred that the introduction of the MF has minimal effect on

478　the distribution of enzymes within the CAZy database.

479　　We conducted a phylogenetic investigation of communities by reconstructing

480　unobserved states (PICRUSt) to validate the effects of the MF on gene function.

481　Functional predictions based on the COG database reveal that genes associated with

482　energy production and conversion, signal transduction, cell wall/membrane/envelope

483　biogenesis and inorganic ion transport exhibit increased expression levels under MF

484　compared to integrated system40-1 (Fig. 6b). This up-regulation in expression can

485 subsequently modulate the relevant metabolic pathways, resulting in alterations in the

486 functional profiles of bacteria.

487 In this study, we employed function prediction based on the Kyoto Encyclopedia of

488 Genes and Genomes (KEGG) database (Fig. 6c). The KEGG database encompasses

489 six significant pathways: (1) metabolism; (2) cellular processes; (3) environmental

490 information processing; (4) genetic information processing; (5) human diseases; and

491 (6) organismal systems. All six metabolic pathways are associated with organic matter

492 degradation. Due to the increased abundance of energy metabolism, amino acid

493 metabolism, signal transduction and membrane transport under the influence of MF,

494 these pathways are further elaborated upon in Fig. 6d. In cellulation processes, the cell

495 viability of microflora under MF surpasses that under NMF conditions. In our study,

496 proteobacteria are the predominant phylum, exhibiting high relative abundance levels.

497 Most bacteria within this phylum possess flagella (Yan et al., 2022). It is possible that

498 under MF, the electron transfer rate through the flagella is accelerated, which may

499 explain the increased motility of these bacteria. Regarding metabolic pathways, MF

500 significantly upregulates the rates of all six pathways. This finding further

501 substantiates that introducing MF can stimulate the production of key enzymes

502 involved in these metabolic processes.

503 Compared to the Universal Protein Resource (UniProt) database, we filtered genes

504 related to the major carbon metabolic pathways in integrated system-1 and system-2

505 on day 40. The carbon metabolism pathway involves the conversion of a carbon

506 source, such as glucose, into pyruvate through a series of enzymatic reactions before

507 entering the TCA cycle (Fig. 7). There are 10 consecutive enzymatic reactions from

508 glucose to pyruvate, with the three most crucial rate-limiting steps being: 1).

509 Glucokinase (EC: 2.7.1.2), which catalyses glucose to glucose-6-phosphate. 2).

510 Fructose-phosphokinase (EC: 2.7.1.11), which catalyses fructose-6-phosphate to

511 fructose-1, 6-diphosphate. 3). Pyruvate kinase (EC:2.7.1.40), which catalyses

512 phosphoenolpyruvate. These reactions are irreversible (Fig. S17). Among them, the

513 abundance of genes encoding these enzymes (EC: 2.7.1.2, EC: 2.7.1.11, and

514 EC:2.7.1.40) in integrated system-1 is higher than in integrated system-2 (Fig. S19).

515 Consequently, pyruvate is synthesised more rapidly, and more carbon sources are

516 consumed in NMF conditions. Citrate synthase (EC:2.3.3.1) catalyses the

517 condensation of acetyl CoA and oxaloacetate to synthesise citrate and CoA (Fig. S18).

518 This step controls entry into the TCA cycle and is a critical rate-limiting step. Genes

519 related to this function are expressed in integrated system-1 and system-2, and no

520 significant difference exists between them (Fig. S20). However, the abundance of

521 genes encoding (EC:2.3.3.1) in integrated system-1 is higher than in integrated

522 system-2. This implies that introducing the MF increases the relative abundance of

523 certain microorganisms within the microbial community during the reaction process.

524 Still, the functional genes related to carbon metabolism do not experience a

525 corresponding increase. Therefore, MF appears to be beneficial for microbial carbon

526 metabolism.

527 *3.5. CIP degradation pathways with MF*

528 To investigate the impact of MF on the intermediates and degradation pathways

529 during the integrated system degradation of CIP, we conducted UPLC-MS tests. Fig. 8

530 illustrates the compounds measured by UPLC during photocatalysis (PC-1 and PC-2

531 products being identical), integrated system-1 and integrated system-2. The

532 UPLC/MS spectra of the detected products can be found in Fig. S21 and Table S3.

533 CIP transforms intermediate compounds with mass-to-charge ratios (m/z) of 348, 316,

534 288 and 291 during photocatalysis alone. These intermediates are identified

535 throughout the entire photocatalytic reaction. Fig. 8 presents the cumulative results

536 obtained after a 12 h reaction time. The findings indicate that photocatalysis cannot

537 further convert these particular aromatic hydrocarbons.

538 In integrated system-2, three intermediates were detected during the 2nd h of the

539 reaction, each with m/z of 274, 263 and 219, respectively. Among these intermediates,

540 the compound with an m/z of 219 originates from the gradual oxidation of the

541 piperazine side chain of CIP, involving the separation and decarboxylation of the

542 secondary amine nitrogen and formaldehyde groups. Conversely, compounds with

543 m/z values of 274 and 263 are generated through the piperazine ring's cleavage and

544 the CO group's loss from the CIP structure. Consequently, the photocatalytic

545 compounds undergo further oxidation during the integrated system process,

546 corroborating our earlier findings (Dong et al., 2023). Additionally, intermediate

547 compounds with m/z values of 274 and 263 also appear in integrated system-1, albeit

548 with longer generation times than integrated system-2. This observation further

549 underscores the capacity of MF to enhance the CIP degradation rate and

550 mineralisation efficiency.

551   In the intermediate reaction stage in integrated system-1, intermediates with m/z

552   values of 245, 154, 274, and 263 are identified. Furthermore, at the end of the reaction,

553   three intermediates with m/z values of 245, 154 and 156 are identified, with the first

554   two intermediates accumulating gradually over the reaction. The structural formulas

555   indicate that these intermediates are aromatic hydrocarbons containing conjugated

556   systems, and their structures exhibit relative stability. Consequently, neither

557   photocatalytic oxidation nor biodegradation in integrated system-1 can facilitate the

558   further degradation of these two intermediates under NMF.

559   During the intermediate reaction stage in integrated system-2, two intermediates

560   with lower molecular weight (M/Z of 148 and 86) were identified. Upon examining

561   their molecular structure formulas, it is evident that these products contain very few

562   double bonds and contain carboxyl groups. These characteristics make them highly

563   susceptible to microbial utilisation for the production of alkane intermediates.

564   Furthermore, no intermediate products were detected in integrated system-2 at the end

565   of the reaction. This finding aligns with the results indicating that the concentrations

566   of TOC and COD in the effluent of integrated system-2 are lower compared to those

567   of integrated system-1.

568   **Conclusions**

569   In general, MF can effectively improve the CIP removal and mineralization rate

570   during integrated photocatalysis and FBBR system. A removal efficiency of ~96% is

571   achieved after 40 days shows the integrated system-2 has outstanding removal

572   efficiency. Moreover, biological involvement increases CIP mineralization rate by

32%. The electrochemical experiment results indicate the charge separation can be promoted by MF, thus increases the electron concentration. Thus, the increase in electron concentration leads to the massive generation of $\cdot OH$ and $\cdot O_2^-$. Moreover, the positive roles of MF on expediting oxidation reactions and increasing microbial respiratory activity and active biomass obviously promote microbial metabolism that leads to diverse compounds. The adaption of the microbial community to MF can alter the microbial community and thus enhance the utilization of the compounds. These actions work together in integrated system-2 to boost CIP degradation and more entire mineralization. To sum up, MF can effectively enhance the CIP degradation and mineralization by integrated system by simultaneously facilitating the charge separation and microbial activity.

References

Albert, L.J., Ravendra, N., 2000. Bioremediation of high molecular weight polycyclic aromatic hydrocarbons: a review of the microbial degradation of benzo[α]pyrene.

596   Int. Biodeter. Biodegr. 45 (1): 57-88.

597   Albuquerque, W.W.C., Costa, R.M.P.B., Fernandes, T.d.S.e., Porto, A.L.F., 2016.

598   Evidences of the static magnetic field influence on cellular systems. Prog. Biophys.

599   Mol. Biol. 121 (1), 16-28.

600   Anwer, H., Park, J.W., 2022. Lorentz force promoted charge separation in a

601   hierarchical, bandgap tuned, and charge reversible $Ni_xMn_{(0.5-x)}O$ photocatalyst for

602   sulfamethoxazole degradation. Appl. Catal. B: Environ. 300, 120724.

603   Cantarel, B.L., Coutinho, P.M., Rancurel, C., Bernard, T., Lombard, V., Henrissat, B.,

604   2009. The carbohydrate-active ENZYMES database (CAZy): an expert resource

605   for glycogenomics. Nucleic Acids Res. 37, 233-238.

606   Ding, R., Yan, W., Wu, Y., Xiao, Y., Gang, H., Wang, S., Chen, L., Zhao, F., 2018.

607   Light-excited photoelectrons coupled with bio-photocatalysis enhanced the

608   degradation efficiency of oxytetracycline. Water Res. 143, 589-598.

609   Dong, Y.L., Xu, D.Y., Wang, Q.W., Zhang, G.M., Zhang, Q.G., Zhang, Z.P., Lv, L.Y.,

610   Xia, Y.G., Ren, Z.J., Wang, P.F., 2021. Tailoring the electronic structure of

611   ultrathin 2D Bi_3O_4Cl sheets by boron doping for enhanced visible light

612   environmental remediation. Appl. Surf. Sci. 542, 148521.

613   Dong, Y.L., Xu, D.Y., Zhang, J., Wang, Q.W., Pang, S.X., Zhang, G.M., Campos, L.C.,

614   Lv, L.Y., Liu, X.Y., Gao, W.F., Sun, L., Ren, Z.J., Wang, P.F., 2023. Enhanced

615   antibiotic wastewater degradation by intimately coupled $B-Bi_3O_4Cl$ photocatalysis

616   and biodegradation reactor: Elucidating degradation principle systematically. J.

617   Hazard. Mater. 445, 130364.

618   Fu, S., Zhao, X., Zhou, Z., Li, M., Zhu, L., 2021. Effective removal of odor

619   substances using intimately coupled photocatalysis and biodegradation system

620   prepared with the silane coupling agent (SCA)-enhanced TiO_2 coating method.

621   Water Res. 188, 116569.

622   Gao, W., Lu, J., Zhang, S., Zhang, X., Wang, Z., Qin, W., Wang, J., Zhou, W., Liu,

623   H., Sang, Y., 2019. Suppressing Photoinduced Charge Recombination via the

624   Lorentz Force in a Photocatalytic System. Adv. Sci. 6, 1901244.

625   Gullert, S., Fischer, M.A., Turaev, D., Noebauer, B., Ilmberger, N., Wemheuer, B.,

626   Alawi, M., Rattei, T., Daniel, R., Schmitz, R.A., Grundhoff, A., Streit, W.R., 2016.

627   Deep metagenome and metatranscriptome analyses of microbial communities

628   affiliated with an industrial biogas fermenter, a cow rumen, and elephant feces

629   reveal major differences in carbohydrate hydrolysis strategies. Biotechnol Biofuels.

630   9, 121.

631   Li, J., Pei, Q., Wang, R., Zhou, Y., Zhang, Z., Cao, Q., Wang, D., Mi, W., Du, Y.,

632   2018. Enhanced Photocatalytic Performance through Magnetic Field Boosting

633   Carrier Transport. ACS Nano. 12, 3351-3359.

634   Ma, Y., Xiong, H.F., Zhao, Z.Q., Yu, Y., Zhou, D.D., Dong, S.S., 2018. Model-based

635   evaluation of tetracycline hydrochloride removal and mineralization in an

636   intimately coupled photocatalysis and biodegradation reactor. Chem. Eng. J. 351,

637   967-975.

638   Nandy, A., Kumar, V., Kundu, P.P., 2013. Utilization of proteinaceous materials for

639   power generation in a mediatorless microbial fuel cell by a new electrogenic

640   bacteria Lysinibacillus sphaericus VA5. Enzym. Microb. Technol. 53 (5), 339-344.

641   Olivares, J., Bernardini, A., Garcialeon, G., Corona, F., Sanchez, M.B., Martinez, J.L.,

2013. The neglected intrinsic resistome of bacterial pathogens. PLoS One 4 (2), e1619.

Sousa, J.C.G., Ribeiro, A.R., Barbosa, M.O., Pereira, M.F.R., Silva, A.M.T., 2018. A review on environmental monitoring of water organic pollutants identified by EU guidelines. J. Hazard. Mater. 344, 146-162.

Strašák, L., Vetterl, V.r., Šmarda, J., 2002. Effects of low-frequency magnetic fields on bacteria Escherichia coli. Bioelectrochemistry 55, 161-164.

Wojcieszynska, D., Guzik, U., Gren, I., Perkosz, M., Hupert-Kocurek, K., 2011. Induction of aromatic ring: cleavage dioxygenases in Stenotrophomonas maltophilia strain KB2 in cometabolic systems. World J. Microbiol. Biotechnol. 27, 805-811.

Yan, H.J., Cui, Y.W., Han, S.C., 2022. Promoting enrichment of sulfur-oxidizing autotrophic denitrifiers via static magnetic fields: Performance and mechanism of magnetic biological effects. Bioresource Technol. 347, 126388.

Yavuz, H., Celebi, S.S., 2000. Effects of magnetic field on activity of activated sludge in wastewater treatment. Enzyme Microb. Technol. 26, 22-27.

Zhang, B., Ji, M., Qiu, Z., Liu, H., Li, J., 2011. Microbial population dynamics during sludge granulation in an anaerobic-aerobic biological phosphorus removal system. Bioresource Technol. 102, 2474-2480.

Zhang, L.L., Xing, Z.P., Zhang, H., Li, Z.Z., Wu, X.Y., Zhang, X.D., Zhang, Y., Zhou, W., 2016. High thermostable ordered mesoporous SiO_2-TiO_2 coated circulating-bed biofilm reactor for unpredictable photocatalytic and biocatalytic performance. Appl. Catal. B: Environ. 180, 521-529.

Zhao, M.Y., Shi, J.L., Zhao, Z.Q., Zhou, D.D., Dong, S.S., 2018. Enhancing

666   chlorophenol biodegradation: Using a co-substrate strategy to resist photo-H_2O_2

667   stress in a photocatalytic-biological reactor. Chem. Eng. J. 352, 255-261.

668   Zhou, D., Xu, Z., Dong, S., Huo, M., Dong, S., Tian, X., Cui, B., Xiong, H., Li, T.,

669   Ma, D., 2015. Intimate coupling of photocatalysis and biodegradation for

670   degrading phenol using different light types: visible light vs UV light. Environ. Sci.

671   Technol. 49, 7776-7783.
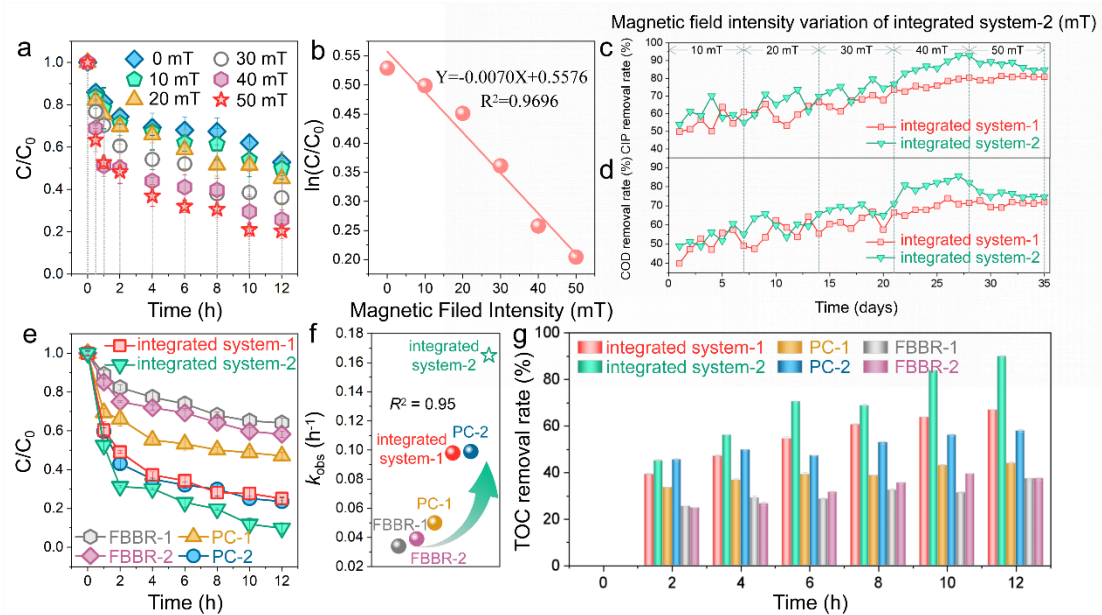
674 **Fig. 1.** (a) The CIP degradation of PC system at different MF intensity. (b) Correlation

675 analysis of external MF strength and CIP degradation efficiency. (c) CIP and (d) COD

676 removal rate of the whole stable operation stage. (e) CIP degradation curves and (f)

677 first-order rate constants of CIP removal under different reaction conditions. (g) TOC

678 removal in an operating cycle with initial CIP concentration of 40 mg/L.

679
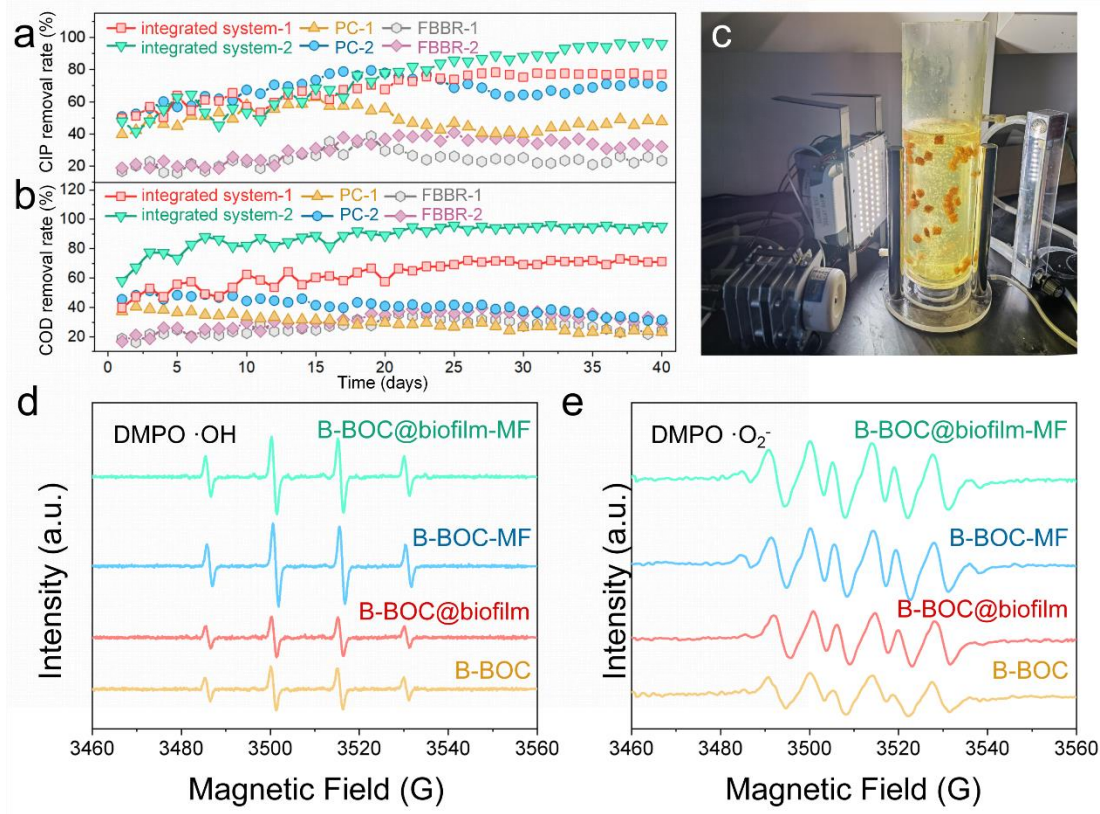
Fig. 2. The removal rate of (a) CIP and (b) COD by integrated system, PC and FBBR under NMF and MF conditions. (c) The photo of CIP (totally 40 mg/L) degradation device. ESR spectra of B-BOC and B-BOC@biofilm with NMF and MF in the existence of (d) DMPO-·OH and (e) DMPO-·O_2^-, respectively.
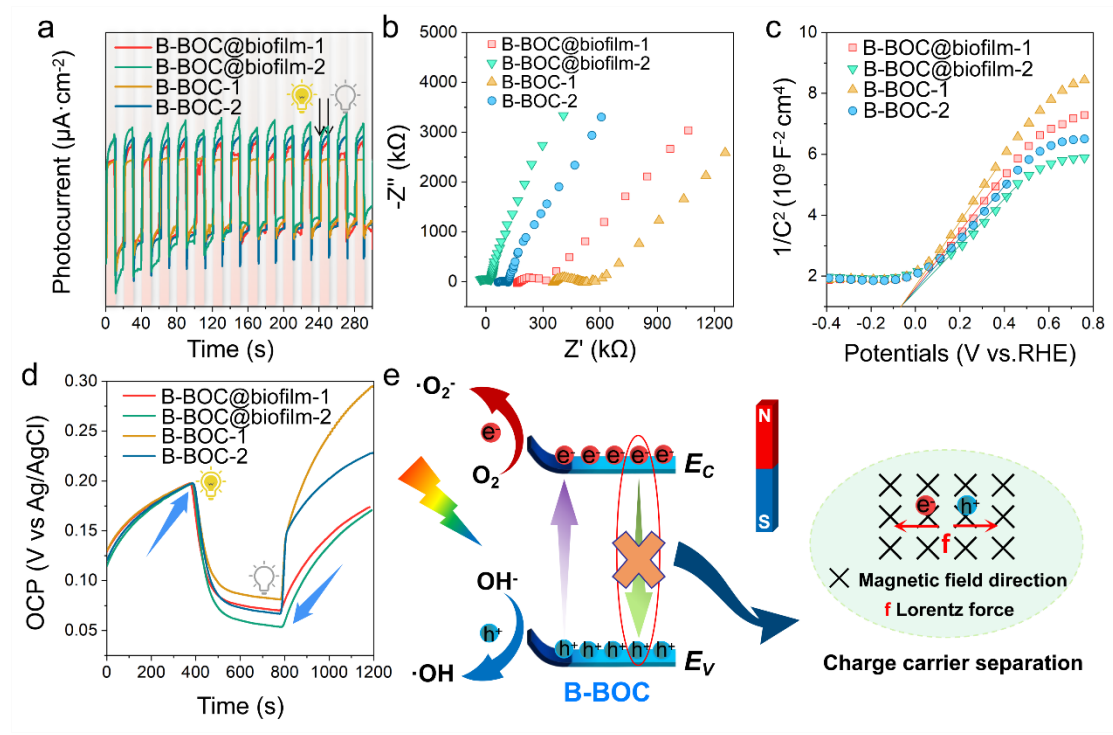
684

685 **Fig. 3.** (a) The I-t curves, (b) EIS, (c) MS and (d) time dependence of open circuit

686 potential of PC and integrated system under NMF and MF conditions. (e) Schematic

687 illustration of proposed photocatalytic mechanism in the B-BOC under MF

688 conditions.

689
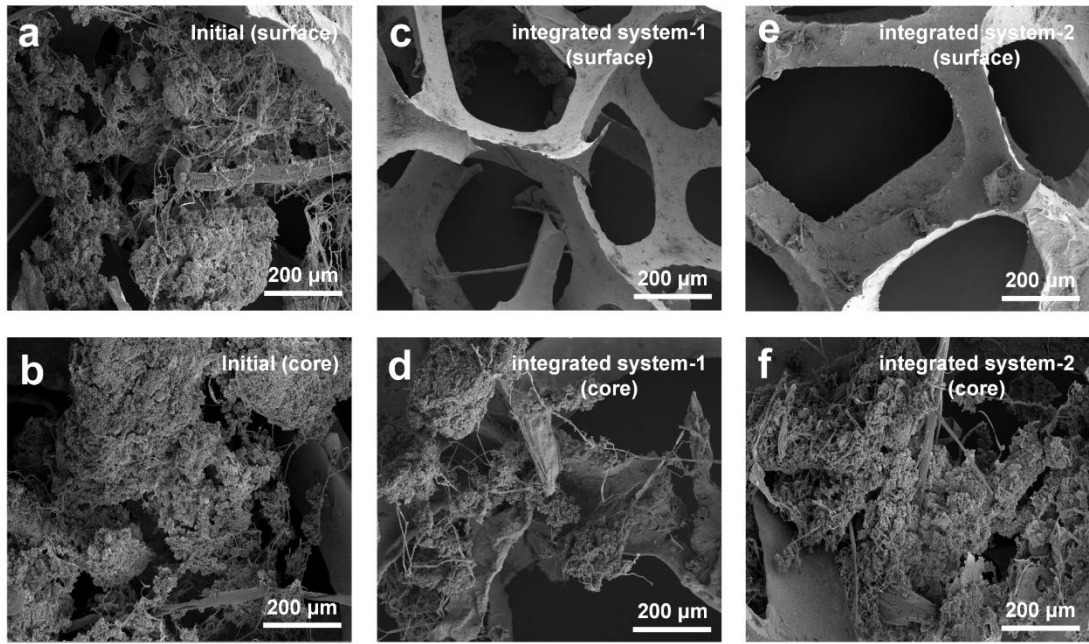
Fig. 4. (a) surface and (b) core of sponge@B-BOC@biofilm, after sponge@B-BOC@biofilm operation for 40 days under (c, d) NMF (integrated system-1) and (e, f) MF (integrated system-2) conditions.
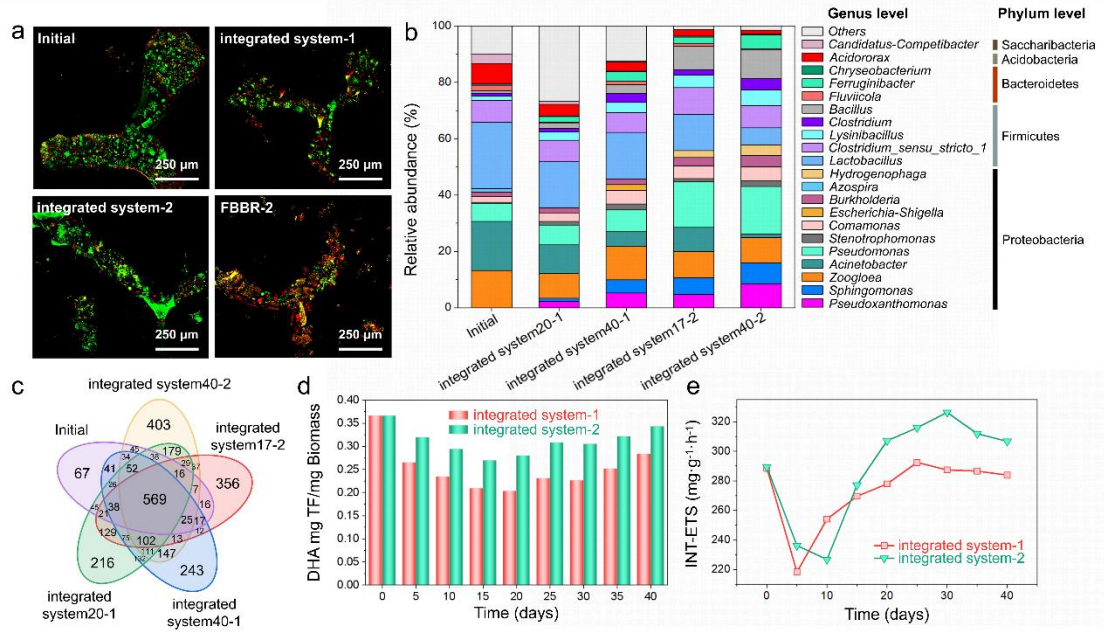
Fig. 5. (a) CLSM images of the photocatalyst-coated biofilm carriers for living cells (green) and dead cells (red) with protocols of integrated system-1, integrated system-2 and FBBR-2. (b) Relative abundances at different operating time in integrated system under NMF (integrated system-1) and MF (integrated system-2) conditions at the phylum and genus levels. (c) Venn diagram of Initial, integrated system20-1, integrated system40-1, integrated system17-2 and integrated system40-2 samples based on ASV. (d) Variation of microbial dehydrogenase activity during CIP degradation by integrated system-1 and integrated system-2. (e) The influence of CIP on microbial activity of ETS.

703
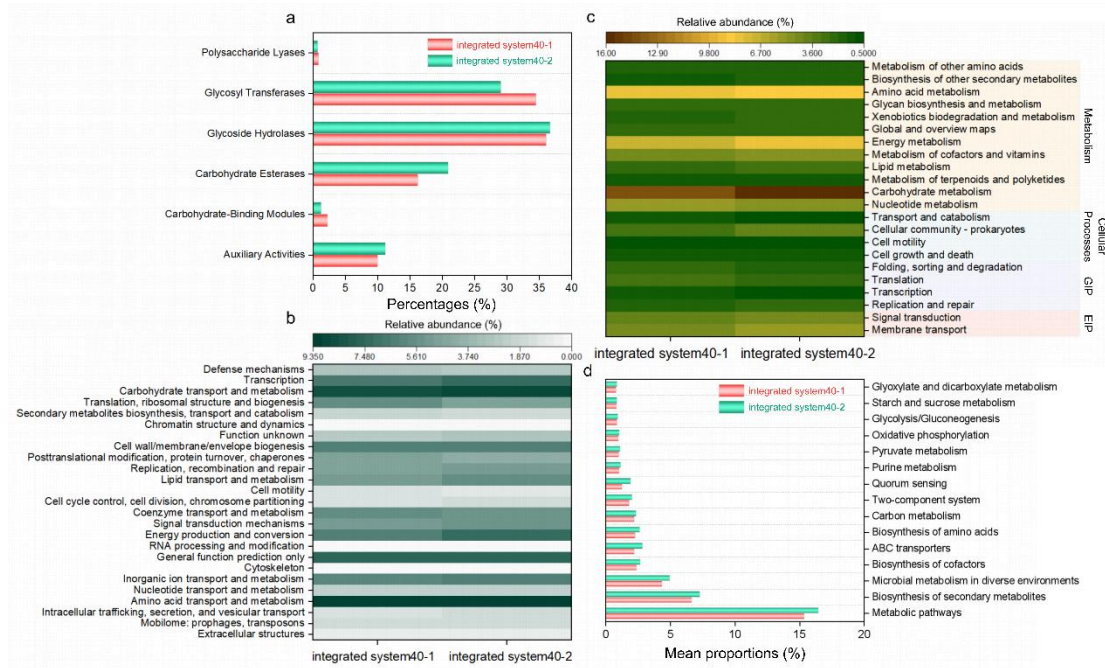
Fig. 6. (a) Gene distribution of CAZy annotation. (b) COG-based function abundances of different samples. (c) PICRUSt prediction based on the KEGG database on microbial function prediction. (d) The potential functional categories of Metabolism (KEGG level 3).
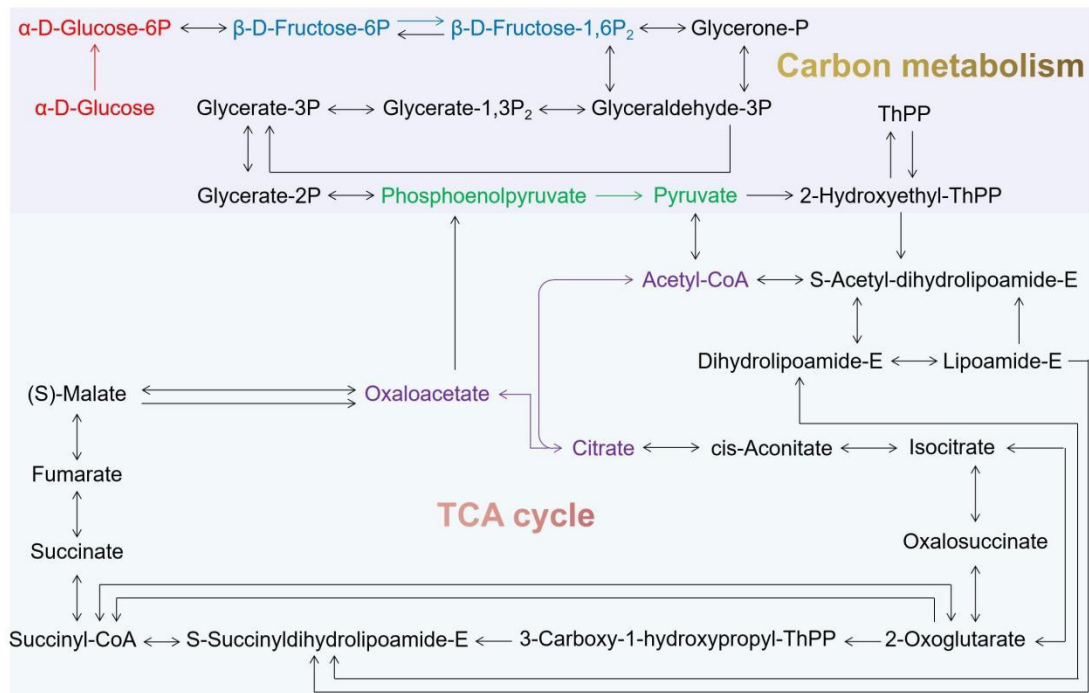
708

709　　　　　　　　　　　**Fig. 7.** Carbon metabolism pathways of biofilms.

710
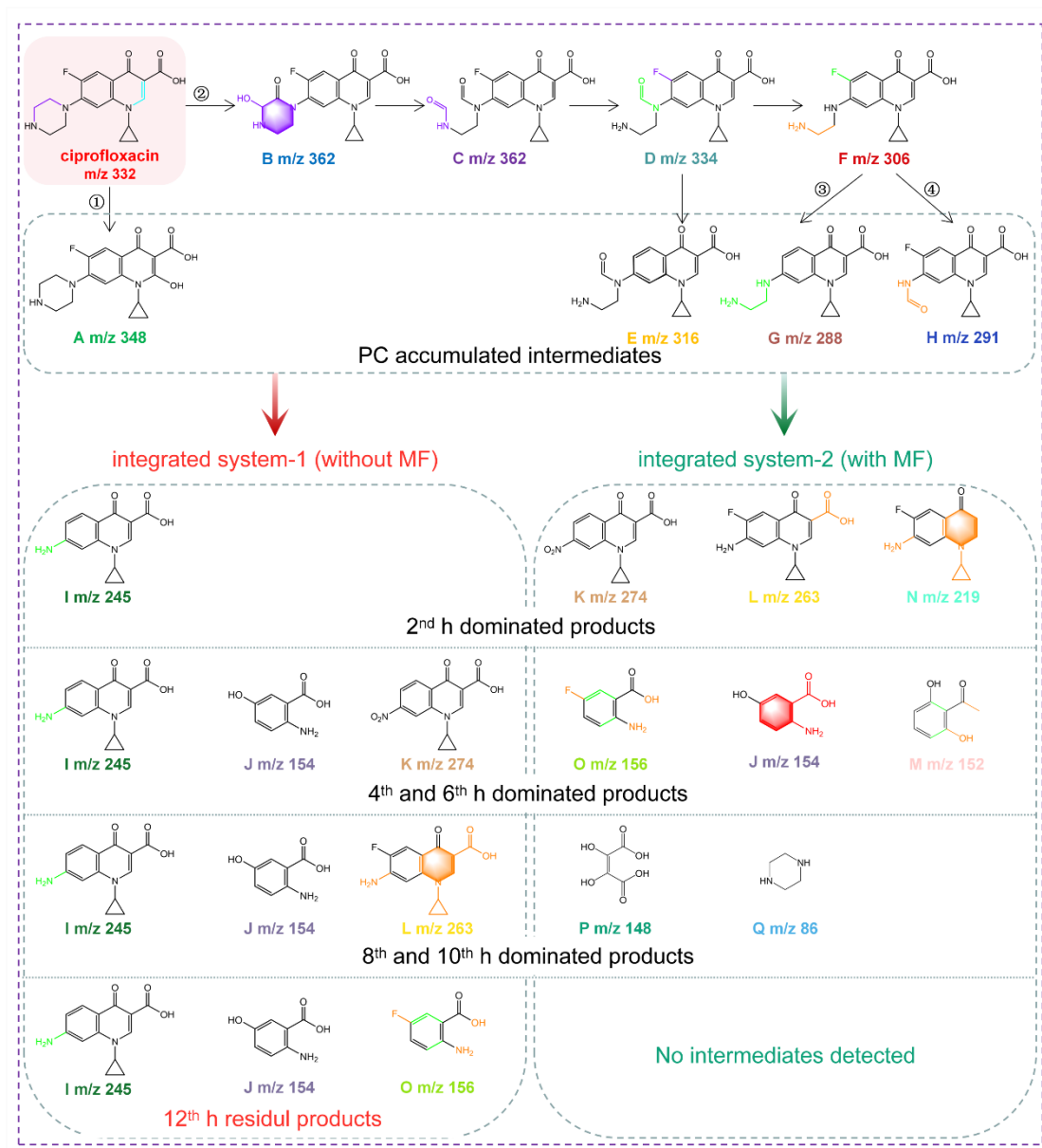
Fig. 8. Proposed CIP-degradation pathways and intermediate products for the protocols under NMF (integrated system-1) and MF (integrated system-2) conditions.

711

712

713

714

715

716

717

718 **Supplementary materials**

719

720 **Dual function of magnetic field in enhancing antibiotic**

721 **wastewater treatment by an integrated photocatalysis and**

722 **fluidized bed biofilm reactor (FBBR)**

723 Yilin Dong [a], Jie Zhang [a], Qiuwen Wang [a], Dongyu Xu [a], Shaoxuan Pang [a], Luiza C.

724 Campos [b], Zhijun Ren [a,*], Pengfei Wang [a,*]

725 a School of Energy and Environmental Engineering, Hebei University of Technology,

726 Tianjin 300401, China

727 b Department of Civil, Environmental and Geomatic Engineering, University College

728 London, London WC1E 6BT, United Kingdom

729 *Correspondence to: Z. J. Ren (E-mail: renzhijun2003@126.com) & P. F. Wang

730 (E-mail: pengfeiwang@hebut.edu.cn)

731

732

733

734

735

736

737

738

739

Text S1. Preparation of B-Bi₃O₄Cl (B-BOC)

Briefly, 0.243 g of $Bi(NO_3)_3 \cdot 5H_2O$, 0.2 g polyvinyl pyrrolidone (PVP, K30) and 0.3 mL H_3BO_3 solution (20 g/L) were diffused into 15 mL mannitol solution (0.1 mol/L) to acquire solution A. Totally, the solution B was obtained by 0.5 mmol NaCl dissolved into 3 mL mannitol solution (0.1 mol/L). Then, solution B and solution A were stirred by magnetic stirrer for 30 min, and adjusted to pH to 11.5 with NaOH solution (2 M). After that, the suspension was sealed in a 50 mL Teflon-lined stainless-steel autoclave, and then the autoclave was kept at 160 °C for 24 h in oven. After cooled down to normal temperature, the solid substances were gathered by centrifugation and washed with deionized water and anhydrous ethanol for three times, respectively, then dried under vacuum at 60 °C all night.

Text S2. Experimental set-up.

CIP degradation was conducted in an internal loop airlift-driven fluidized bed reactor with a working volume of 800 mL. The reaction device is made of plexiglass, which is mainly composed of two inner and outer hollow cylinders. The height of the outer hollow cylinder is 220 mm, and the outer diameter and inner diameter are 100 mm and 90 mm, respectively. The height of the inner concentric annular column is 170 mm, the outer diameter and inner diameter are 60 mm and 50 mm, respectively, and four 20 mm×20 mm rectangular channels are set at the bottom. The inner annular cylinder is nested in the annular space between the outer annular cylinder and the bottom aeration disc. The bottom of the reactor is provided with an aeration disc with the same diameter as the inner wall sleeve.

Text S3. Analytical methods

784

785   The morphology of B-BOC was observed by using an SU8000 scanning electron

786   microscope (SEM, Hitachi, Japan) at an accelerating voltage of 3-5 kV and a Tecnai

787   G20 (FEI Co., Holland) microscope operated at an accelerating voltage of 200 kV.

788   The transmission electron microscopy (TEM) images were tested using Tecnai G2

789   and FEI Co to acquire morphology of the photocatalysts. Powder X-ray

790   diffractometry (XRD) was obtained by a Bruker D8 diffractometer with Cu Kα

791   radiation. X-ray photoelectron spectroscopy (XPS) was collected by a 5300

792   ESCALAB spectrometer to explore the surface chemical element. UV-Vis absorption

793   spectra of the photocatalysts were proceeded using a UV-vis spectrophotometer

794   (U-3900H, Shimadzu). The electron spin resonance (ESR) signals were tested by

795   using a Bruker EPR JES-FA300 instrument to obtain the activated species.

796   Photo-electrochemical characterizations were carried out in a standard three-electrode

797   system by an electrochemical station (CHI660D) with a blank or modified stainless

798   steel wire (1.0×1.5 cm) as the working electrode, the carbon rod as the counter

799   electrode, and the Hg/Hg_2Cl_2 electrode as the reference electrode. The electrolyte was

800   0.5 M $NaSO_4$ solution. Moreover, the light density employed was 80 mW/cm^2.

801   The microstructure of the biofilm during CIP removal was observed by scanning

802   electron microscopy (SEM). Details of the sample pretreatment method are provided

803   in Text S4. Pretreatment procedures for biofilm staining process for confocal laser

804   scanning microscopy (CLSM) imaging are provided in Text S5. The total organic

805   carbon (TOC) was measured using a TOC analyzer (Shimadzu, Japan). COD analysis

was measured using a COD quick detector (LianHua Tech-Co., Ltd., China). The biofilm samples were collected from each integrated system every five days to measure for Dehydrogenase Activity (DHA) and electron transport system (ETS) activity. DHA and ETS were determined by triphenyltetrazolium chloride (TTC) colorimetry and the 2-(p-iodophenyl)-3-(p-nitrophenyl)-5-phenyltetrazolium chloride electron transport system (INT-ETS), respectively. Their specific measurement steps are provided in Texts S6 and S7, respectively.

828 **Text S4. Pretreatment for SEM observation**

829   Biofilm samples attached to carriers were prepared for SEM by washing them with

830 0.01 M phosphate buffered saline (PBS) and fixing them with 2.5% (wt)

831 glutaraldehyde for 30 min, and then frozen at -20 °C. We visualized interior of the

832 carriers by slicing the carriers with a sterile razor blade prior to gold coating and then

833 observed with an SEM instrument (JSM-7500F; Japan).

834

835

836

837

838

839

840

841

842

843

844

845

846

847

848

849

Text S5. Staining and confocal laser scanning microscopy (CLSM) imaging

850

851   The carrier samples attached with biofilm were washed with PBS for three times,

852   fixed with 4 wt% paraformaldehyde at 4 °C for 4 h, and then washed with PBS again.

853   Then the pretreated samples were frozen and sliced. Followed by staining using

854   staining activity assay kit (L-7012, LIVE/DEAD® BacLight TM, USA). The sections

855   were then placed on microscope slides and analysed using a CLSM instrument

856   (LEICA TCS SP5, Germany).

857

858

859

860

861

862

863

864

865

866

867

868

869

870

871

Text S6. Measurement of Dehydrogenase Activity (DHA)

First, 20 sponge carriers were removed from the reactor and placed in a 50 mL centrifuge tube. Add 2.5 mL distilled water, 5 mL TTC solution (4 mg/mL), 2 mL glucose solution (0.1 mol/L) and 2 mL Tris-HCl buffer solution (7.874 g/L, pH = 8.4) successively. Put the centrifuge tube into an oscillator (200 rpm) and shake for 20 min. Then put it into a constant temperature incubator (37 ℃) for 1 h, and drop concentrated sulfuric acid to terminate the reaction. Finally, triphenylmethane (TC) in the solution was extracted with 5 mL toluene, and the centrifuge tube was placed in an oscillator to vibrate (200 rpm) for 30 min before ultrasonic treatment 8 min. The mixed solution is centrifuged at the speed of 4000 rpm for 5 min after standing for 3 min. The supernatant is taken to measure its absorbance at 485 nm. The dehydrogenase activity of the sample can be obtained by comparing with the standard curve.

894

Text S7. Measurement of electron transport system (ETS)

Add 0.3 mL of sludge mixture, 1.5 mL of Tris-HCl buffer solution, and 1 mL of 0.2%

INT solution in sequence to the 10 mL centrifuge tube. The prepared samples were

rapidly cultured in a dark oscillator at 37 ± 1°C for 30 min, and then 1 mL of 37%

formaldehyde was added to terminate the reaction. Centrifuge at 4000 r/min for

another 5 min, the supernatant gently discarded, 5 mL methanol added, mixed and

stirred evenly, and continued to oscillate and extract at 37 ± 1°C in the dark for 10

min, centrifuge for another 5 min at 4000 r/min. The absorbance of the extract was

measured at 485 nm by a spectrophotometer. The calculation formula of INT-ETS is

as follows:

$$U^T = \frac{D_{485}V}{K_T V_M t}$$

U^T: activation of INT-ETS, mg·(g·h)$^{-1}$; D_{485}: absorbance of supermate (wavelength =

485 nm); V: volume of extract liquor, mL; K_T: slope of standard curve (K_T = 0.0475

L/mg); V_M: volume of the mixture, mL; t: culture time, h

916

917

Table S1. First-order loss rates of CIP (k) based on First-order kinetic simulation in
PC and integrated system under NMF and MF.

	k/h^{-1}	R^2
PC-1	0.050	0.87
PC-2	0.099	0.90
integrated system-1	0.098	0.91
integrated system-2	0.165	0.95

920

921

922

923

924

925

926

927

928

929

930

931

932

933

934

935 **Table S2.** Richness and diversity indices obtained by high throughput sequencing.

Samples	Chao1 indexes	ACE indexes	Simpson indexes	Shannon indexes
Initial	1403	1729	0.066	4.51
integrated system40-1	1782	2069	0.053	8.01
integrated system40-2	2003	2264	0.038	9.04

936

937

938

939

940

941

942

943

944

945

946
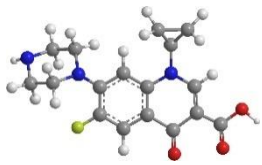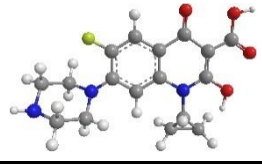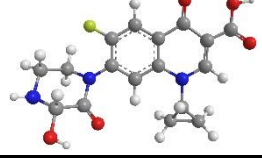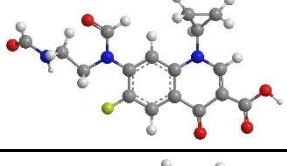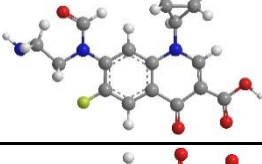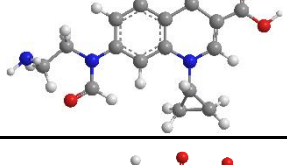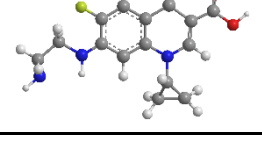
947
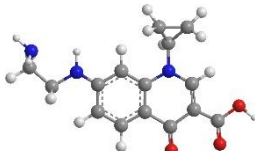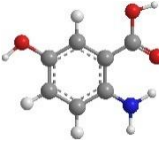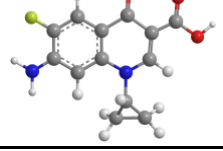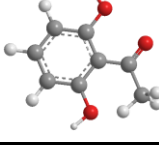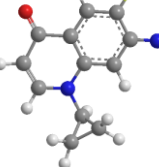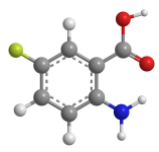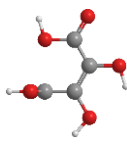
948

949

950

951 **Table S3.** Identification of the possible CIP degradation products by LC-MS under

952 visible light irradiation.

Compounds	Formula	m/z	Proposed structure
CIP	$C_{17}H_{18}FN_3O_3$	332	
A	$C_{17}H_{18}FN_3O_4$	348	
B	$C_{17}H_{16}FN_3O_5$	362	
C	$C_{17}H_{16}FN_3O_5$	362	
D	$C_{16}H_{16}FN_3O_4$	334	
E	$C_{16}H_{17}N_3O_4$	316	
F	$C_{15}H_{16}FN_3O_3$	306	

G	$C_{15}H_{17}N_3O_3$	288	
H	$C_{14}H_{11}FN_2O_4$	291	
I	$C_{13}H_{13}N_2O_3$	245	
J	$C_7H_7NO_3$	154	
K	$C_{13}H_{10}N_2O_5$	274	
L	$C_{13}H_{11}FN_2O_3$	263	
M	$C_8H_8O_3$	152	
N	$C_{12}H_{11}FN_2O$	219	
O	$C_7H_6FNO_2$	156	
P	$C_4H_4O_6$	148	

Q	$C_4H_{10}N_2$	86	
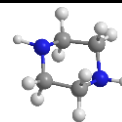
953
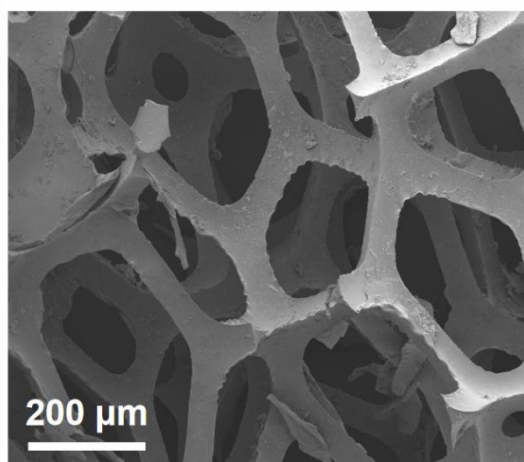
954

955 **Fig. S1.** SEM images of sponge.

956   SEM image shows the surface morphology of the sponge carrier is a network

957 skeleton with 300~800 μm macropores and large specific surface area (Fig. S1).

958

959

960

961

962

963

964

965
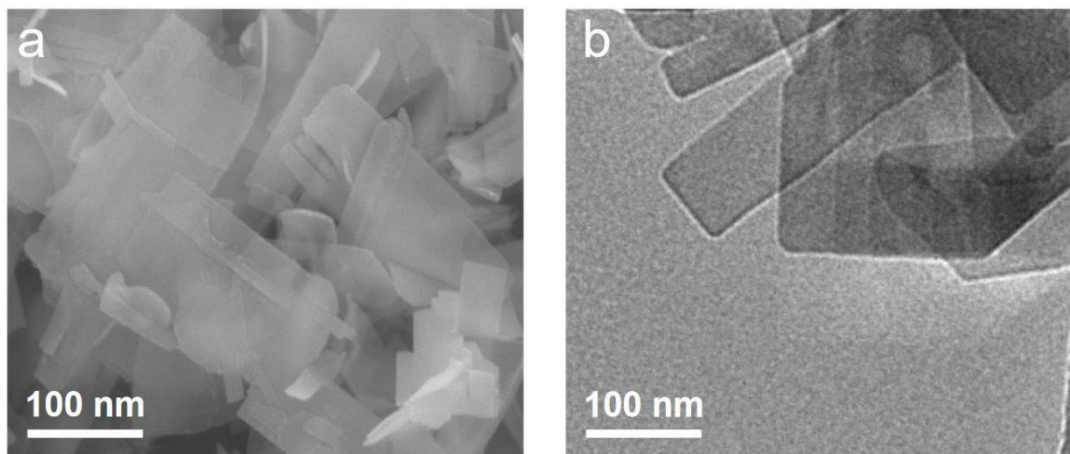
966

967 **Fig. S2.** (a) SEM and (b) TEM images of B-BOC nanosheets.

968   The morphology of B-BOC was analyzed by scanning electron microscopy (SEM)

969 and transmission electron microscopy (TEM) (Fig. S2), from which the nanosheets

970 with a lateral size of one hundred to several hundreds of nanometers can be observed.

971

972

973

974

975

976

977

978

979

980

981

982
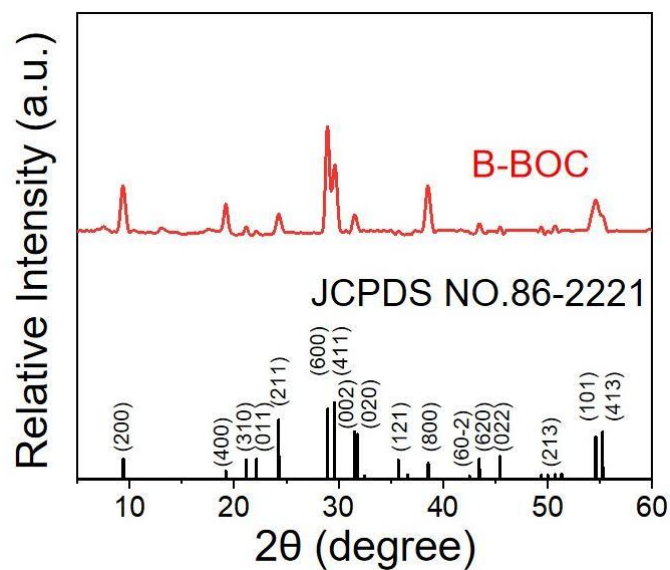
Fig. S3. XRD patterns of B-BOC.

In Fig. S3, the X-ray diffraction (XRD) peaks of the B-BOC nanosheet reveal a pure monoclinic BOC crystal phase (JCPDS No. 86-2221) with layered structure (Li et al., 2016). Moreover, there is no other impurity phases observed, which indicates that B doping does not alter the crystal phase.

999
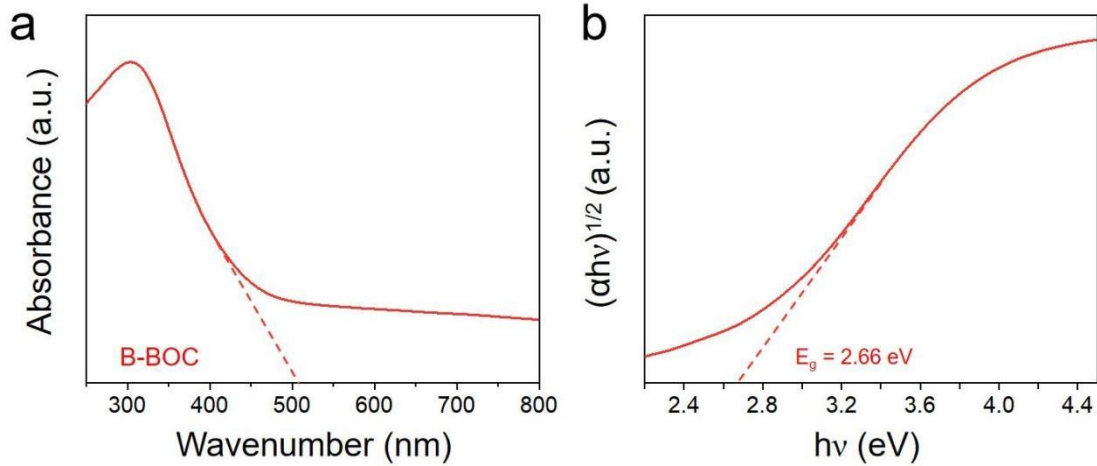
Fig. S4. (a) Ultraviolet-visible diffuse reflectance spectra and (b) the band gap energy (Eg) of B-BOC.

The photoabsorption performance and energy band characteristic of the B-BOC nanosheet were implemented by UV-vis diffuse reflectance spectroscopy (DRS) as showed in Fig. S4a. It is worth noting that an extensive light absorption of B-BOC can be examined in the visible light range, and the absorption fringe approximately at 503 nm. Attentively, the energy gap of B-BOC is 2.66 eV, resulting B-BOC has a wide light absorption of visible light (Fig. S4b).
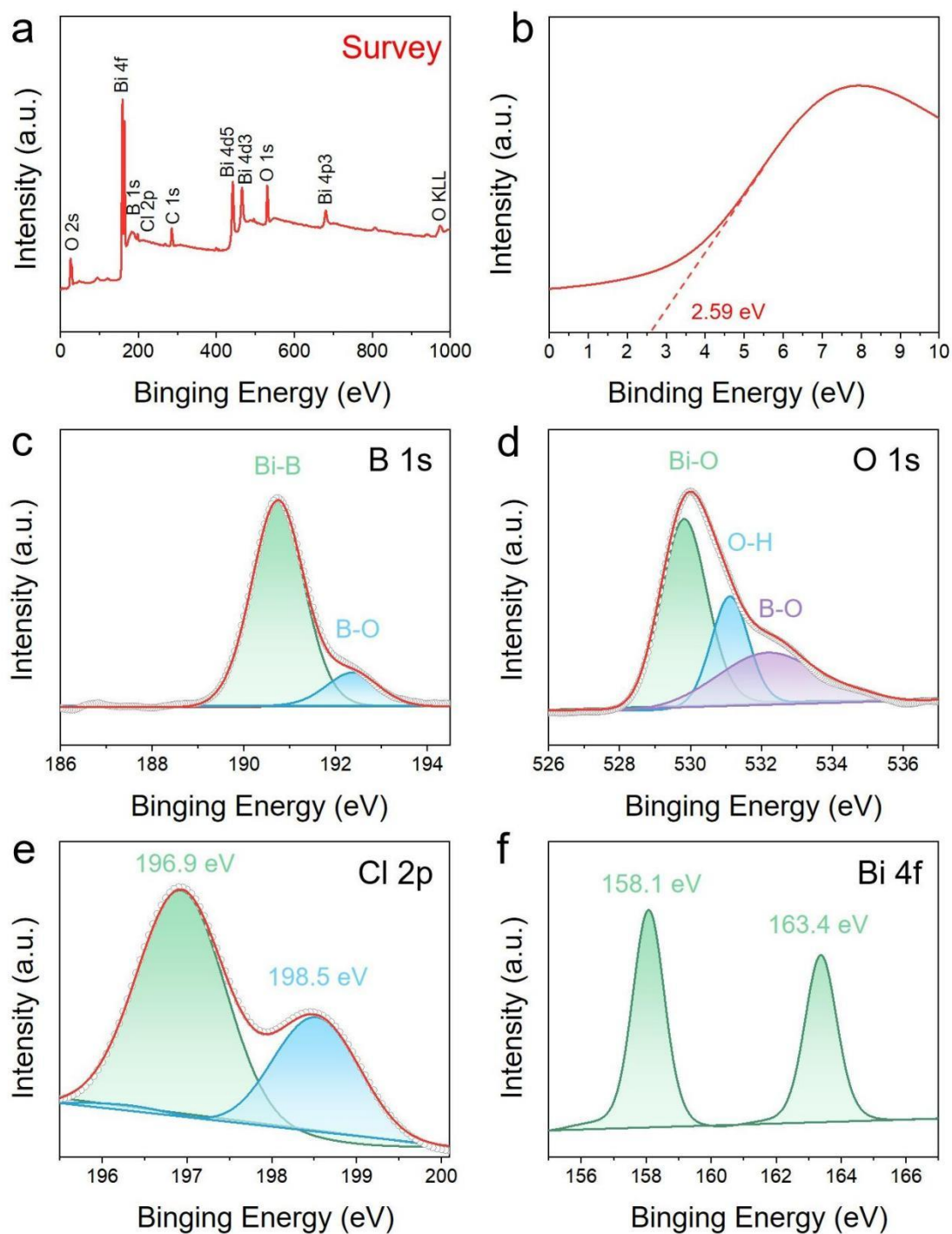
Fig. S5. (a) XPS survey spectra, (b) valence-band (VB) spectra, (c) B 1s spectra, (d) O 1s spectra, (e) Cl 2p spectra, (f) Bi 4f spectra of the B-BOC.

The XPS survey spectra indicates that all the elements of Bi, O, Cl and B are presented in the B-BOC (Fig. S5a), which is in accordance with XRD results. Moreover, the VB of photocatalyst is measured by XPS valence spectra (Fig. S5b).

1022 And the VB maximum of B-BOC is assessed to be 2.59 eV. For B 1s, the peaks are

1023 observed at binding energy of 190.7 eV and 192.5 eV for B-BOC, which assign to the

1024 Bi-B bonds and B-O bonds, respectively (Fig. S5c) (Yu et al., 2019). Furthermore, the

1025 O 1s peaks situate at 529.8 eV, 531.2 eV and 532.2 eV can be corresponded to Bi-O

1026 bonds, O-H bonds and B-O bonds, respectively (Fig. S5d) (Yang et al., 2016). Then,

1027 for Cl 2p, the peaks at 198.52 eV and 196.9 eV are equivalent to the $2p_{3/2}$ and $2p_{1/2}$

1028 orbitals of Cl^-, respectively (Fig. S5e). Furthermore, Bi 4f spectra display two peaks at

1029 163.31 eV and 158.08 eV, assign to the Bi $4f_{5/2}$ and Bi $4f_{7/2}$ (Fig. S5f). Therefore, the

1030 above results indicate that the successful synthesis of B-BOC photocatalyst.

1031

1032

1033

1034

1035

1036

1037

1038

1039

1040

1041

1042

1043
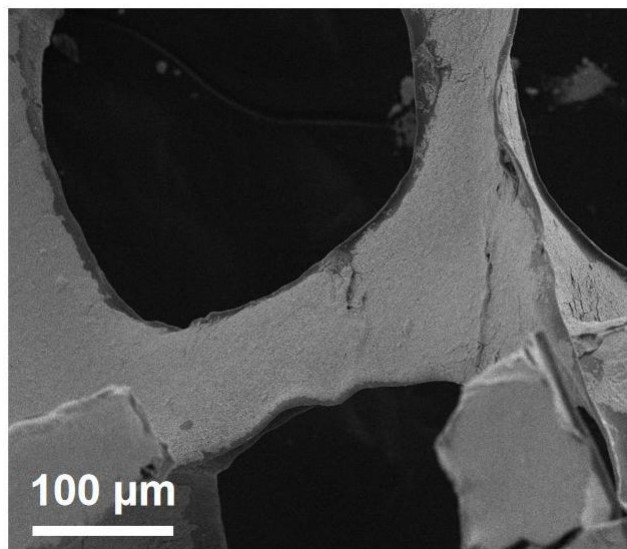
Fig. S6. SEM images of sponge@B-BOC.

1044

1045

Moreover, Fig. S6 demonstrates the B-BOC photocatalysts are uniformly and

1046

densely attached to the bone surface of the sponge carrier, its original network

1047

skeleton is fully preserved.

1048

1049

1050

1051

1052

1053

1054

1055

1056

1057

1058
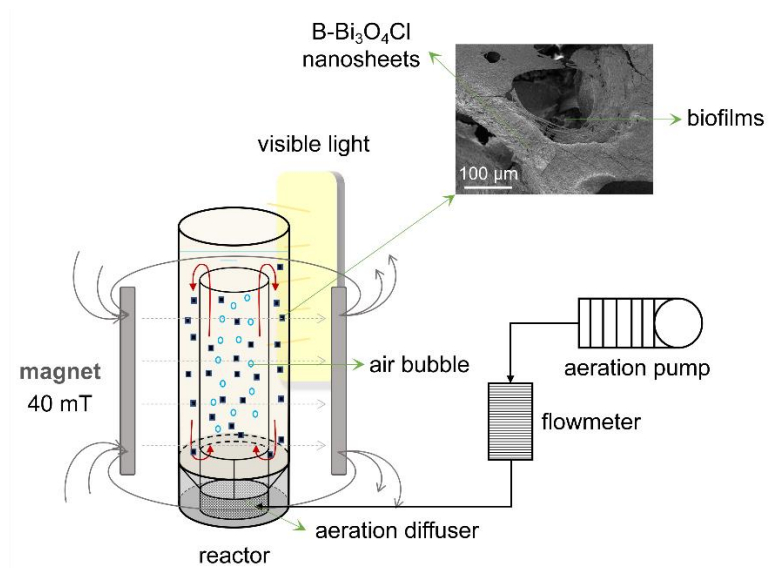
1059

1060   **Fig. S7.** Schematic diagram of the photocatalytic circulating-bed biofilm reactor with

1061   MF.

1062

1063

1064

1065

1066

1067

1068

1069

1070

1071

1072
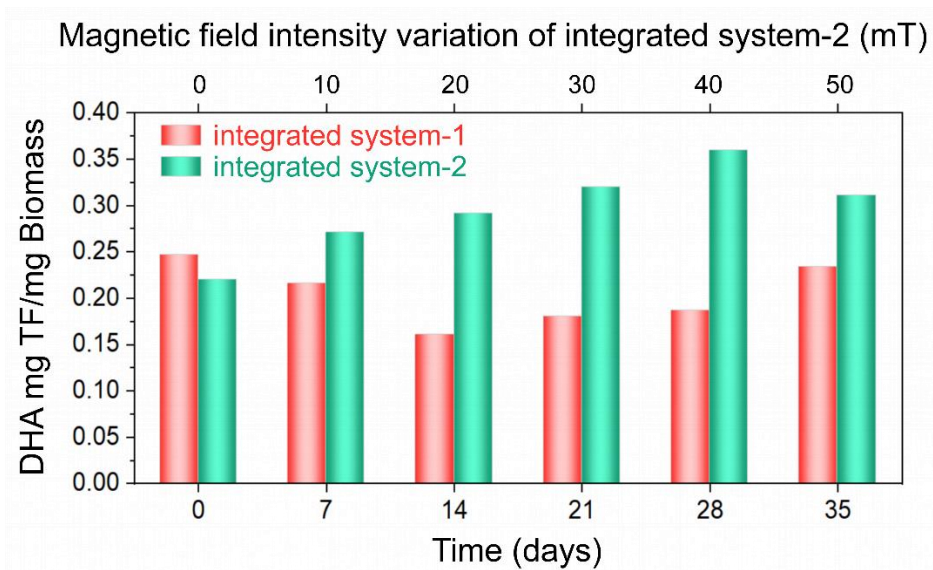
Fig. S8. Microbial dehydrogenase activity in integrated system-1 and integrated system-2 reactors.

Microbial dehydrogenase activity (DHA) can reflect the degradation efficiency of substrate under different MF intensity. Fig. S8 shows the variation trend of DHA as MF intensity in integrated system-1 and integrated system-2 reactors. The enzyme activity of integrated system-2 increases first and then decreases, and MF enhanced DHA is higher than integrated system-1 at all intensities. At the intensity of 40 mT, MF has the most significant strengthening effect, and integrated system-2 has the maximum strengthening activity of 0.36 mgTF/mgSS compared with integrated system-1 with 0.19 mgTF/mgSS. Obviously, the suitable MF intensity is helpful to improve the microbial DHA and the degradation efficiency of the substrate. MFs exerts a significant force effect on enzyme activity by influencing metal ions at the enzyme active site. It is found that weak MF has a positive catalytic effect on enzyme activity, depending on the type and structure of the enzyme. MF strength can achieve greater enhancement efficiency of microbial activity.
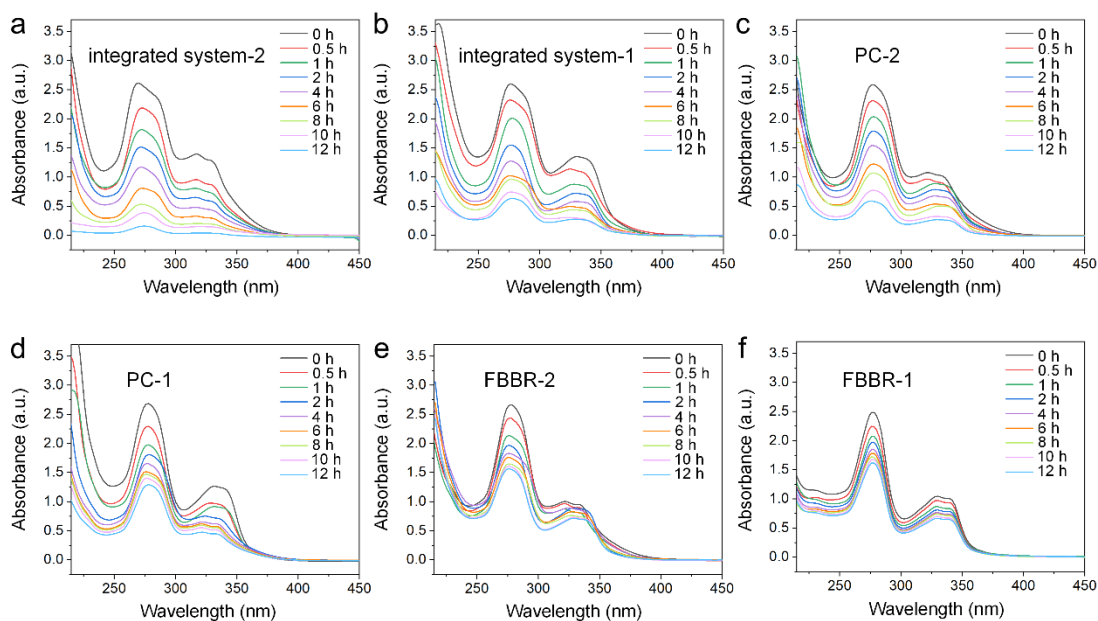
Fig. S9. Changes of UV-vis spectra of CIP solutions in (a) integrated system-2, (b) integrated system-1, (c) PC-2 (d) PC-1 (e) FBBR-2 and (f) FBBR-1 along the operating time of 12 h.

Fig. S9 shows the UV-vis full scanning spectra of CIP degradation in integrated system, PC and FBBR at different times under NMF and MF. For individual biological reactions, the adsorption rate of FBBR-1 to CIP is low, but do not significantly improve after applied MF, indicating the toxic effect of CIP on microorganisms. The removal rate of PC-2 to CIP is significantly higher than that of PC-1, indicating that the Lorentz force produced from MF can effectively inhibit the recombination of photogenerated carriers, and ultimately improve the degradation efficiency of PC-2 to CIP. In integrated system-1, the absorbance of CIP solution at 278 nm decreases with the reaction. However, when MF is applied to integrated system, we find that the absorbance drop rate of CIP solution at 278 nm in integrated system-2 increases. The results indicate that MF has a certain effect on the

1104 photocatalytic degradation of CIP, and a certain magnetic induction intensity

1105 promotes the microbial activity and oxidase in activated sludge, thus enhancing the

1106 CIP degradation rate.
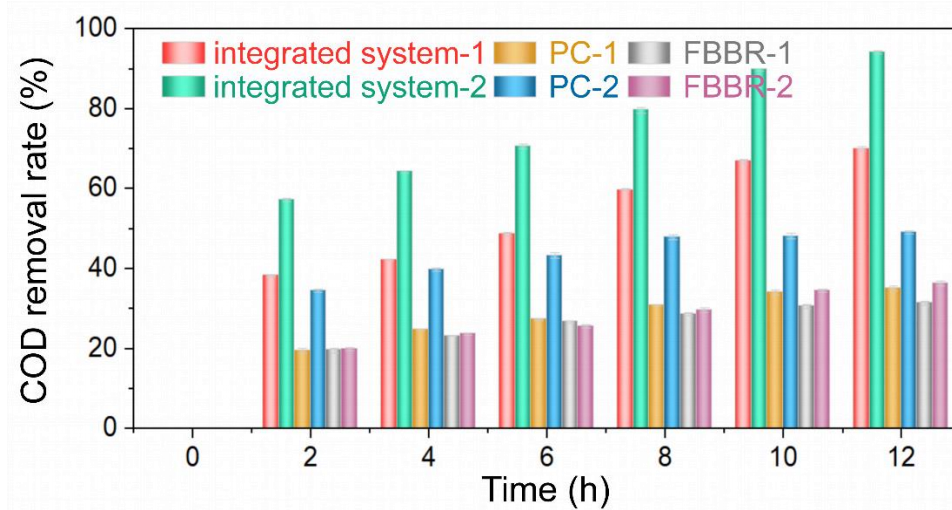
1107

1108 **Fig. S10.** COD removal in an operating cycle with initial CIP concentration of 40

1109 mg/L.

1110 As can be seen from Fig. S10, the applied MF hardly increases the mineralization

1111 rate of CIP by individual organisms when the initial concentration of CIP is 40 mg/L.

1112 The mineralized efficiency of CIP in PC-1 is only 35.0%, indicating that

1113 photocatalytic oxidation alone has poor mineralized efficiency of CIP. However, PC-2

1114 improves the mineralization rate of CIP. After coupled biodegradation, integrated

1115 system-1 increases CIP mineralization efficiency by 34.91% compared with PC-1.

1116 This demonstrates the use of intermediates by organisms in integrated system. In

1117 addition, integrated system-2 increases COD removal rate by 24% compared with

1118 integrated system-1. This indicates that applying MF in integrated system can

1119 improve the mineralization efficiency of CIP.

1120

1121

1122
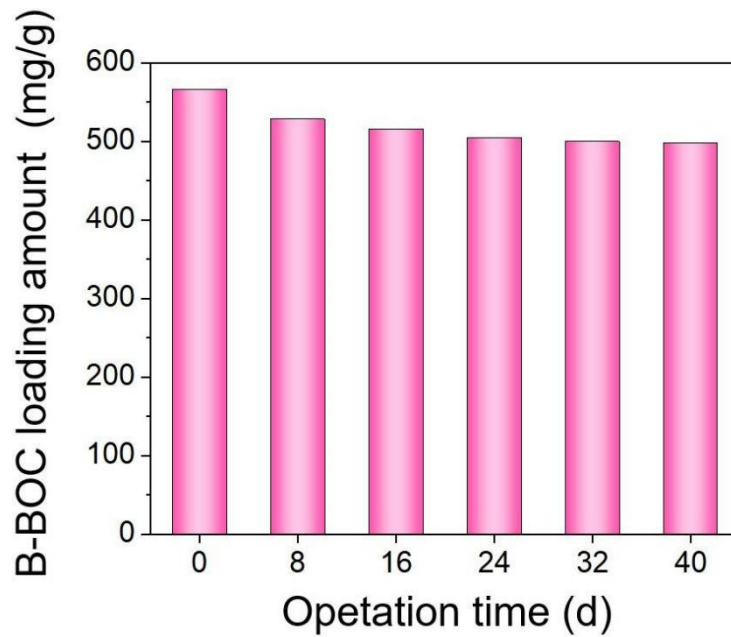
1123

Fig. S11. B-BOC loading amount on the surface of carrier after 40 days of operation.

After 40 days of continuous operation, the loading amount is slightly reduced from the initial 566.1 mg/g to 497.7 mg/g, resulting in a peeling ratio as low as 12.1%. These results further confirm B-BOC are well attached to sponge carrier, indicating that integrated system-2 have good stability. This is beneficial to the long-term operation of integrated system-2.

1130

1131

1132

1133

1134

1135

1136

1137
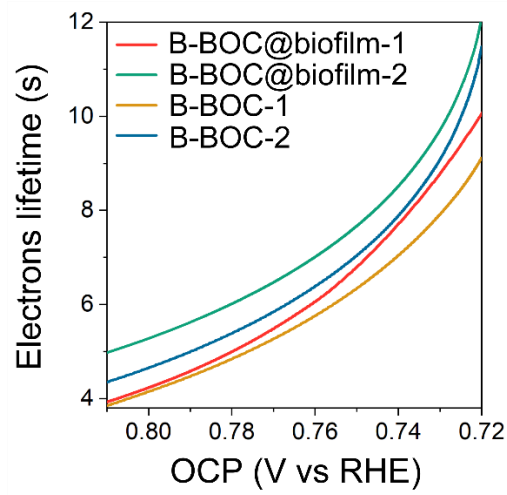
Fig. S12. Electron lifetime as a function of open-circuit potential.

The OCPD rate is directly relevant to the electron lifetime with the following formula:

$$\tau = \frac{-k_B T}{e}\left(\frac{dV_{OC}}{dt}\right)^{-1}$$

Where, k_B is Boltzmann's constant, T is the temperature, and e is the elementary charge.

1152

1153
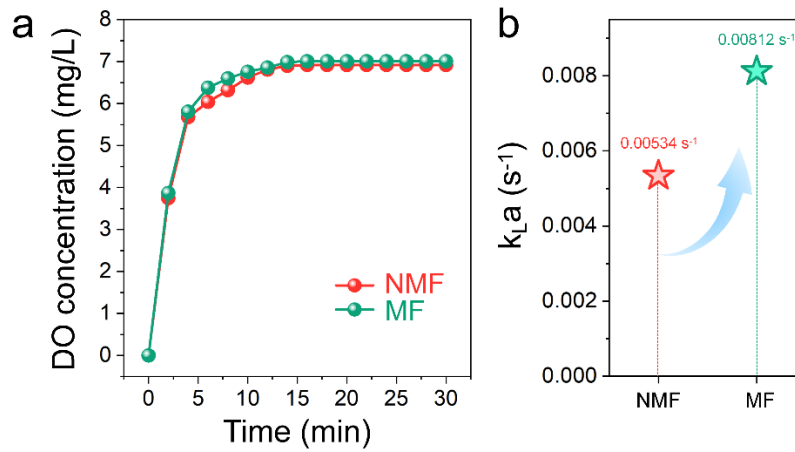
1154

Fig. S13. (a) The changes of dissolved oxygen (DO) for water with air inlet time

under NMF and MF conditions. (b) Volume mass transfer coefficient of oxygen-water

vapor-liquid two phases under NMF and MF conditions.

Volumetric gas-liquid mass transfer coefficient (k_La) measurements were measured

by the dynamic gassing-in method (Gogate and Pandit, 1999). In this method, the DO

concentration in the water was initially reduced to zero by sparging nitrogen gas. The

system was then kept stationary for a few minutes so that all the nitrogen bubbles

were allowed to escape from the liquid. Under NMF and MF conditions, air was

added into the system. The difference of dissolved oxygen concentration with time

was recorded by a dissolved oxygen meter every 2 min until the liquid is almost

saturated by oxygen.

The oxygen-water-gas-liquid mass transfer coefficient k_La of two-phase volume

could be measured based on the equation from the literature (Kumar et al., 2005).

The equation for the oxygen absorption rate:

$$\frac{d\rho}{dt} = K_L a(\rho_g{}^* - \rho_L)$$

1169

1170   Integrate to the above equation to obtain $k_L a$:

$$K_L a = -\frac{1}{t - t_0} ln(\frac{\rho_g{}^* - \rho_L}{\rho_g{}^* - \rho_{L0}})$$

1171

1172   where, $k_L a$ is the volumetric mass transfer coefficient (s^{-1}), t is time (s), $\rho_g{}^*$ is the

1173   dissolved oxygen saturation concentration (mg/L), ρ_L is the dissolved oxygen

1174   concentration at any time (mg/L) and ρ_{L0} is the initial dissolved oxygen concentration

1175   (mg/L).

1176   Through mathematical transformation:

$$ln(\frac{\rho_g{}^* - \rho_L}{\rho_g{}^* - \rho_{L0}}) = K_L a(t_0 - t)$$

1177

1178   Therefore, with t as the abscissa and $ln((\rho_g{}^* - \rho_L)/(\rho_g{}^* - \rho_{L0}))$ as the ordinate, a straight

1179   line can be obtained, and the slope is $k_L a$.

1180

1181

1182

1183

1184

1185
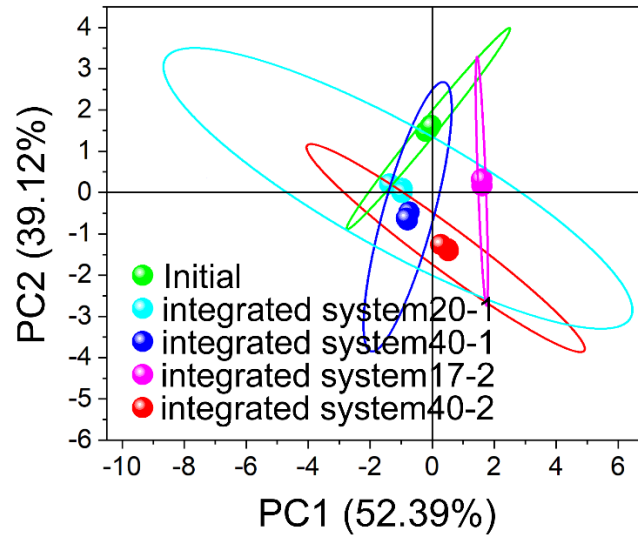
1186
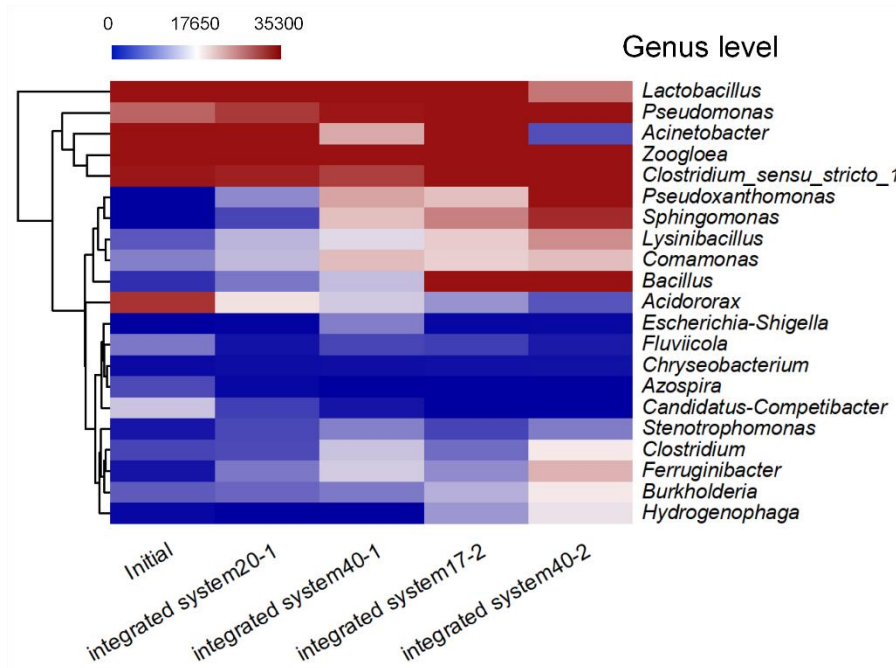
Fig. S14. Pyrosequencing results of DNA from the microbial community of Initial, integrated system20-1, integrated system40-1, integrated system17-2 and integrated system40-2 samples at the genus levels.

The heat map (Fig. S14) clearly shows the evolution of the microbial community at the genus level. *Pseudoxanthomonas* and *Sphingomonas* emerge after the degradation process, indicating adaptation to the intimately coupled environment. *Lysinibacillus*, *Pseudomonas*, *Burkholderia*, and *Bacillus* are all very abundant and have the ability to transfer extracellular electrons, revealing the potential of photoelectron transfer between microorganisms and photocatalysts. Moreover, the number of bacteria increases significantly after applying MF, indicating that MF can effectively promote electron transfer.

PC2 (39.12%)

PC1 (52.39%)

Initial
integrated system20-1
integrated system40-1
integrated system17-2
integrated system40-2

1202

Fig. S15. Principal component analysis (PCA) analyses of samples.

PCA was used to determine the correlation of five activated sludge samples. The closer the samples are, the more similar the species composition structure will be. Therefore, the samples with highly similar community structure will be closer in the figure, while the samples with large community differences will be farther apart. It can be seen from Fig.S15 that the integrated system40-2 sample is significantly different from the Initial sample, indicating that the MF has an effect on the structural changes of the biological community in the reactor.

1203

1204

1205

1206

1207

1208

1209

1210

1211
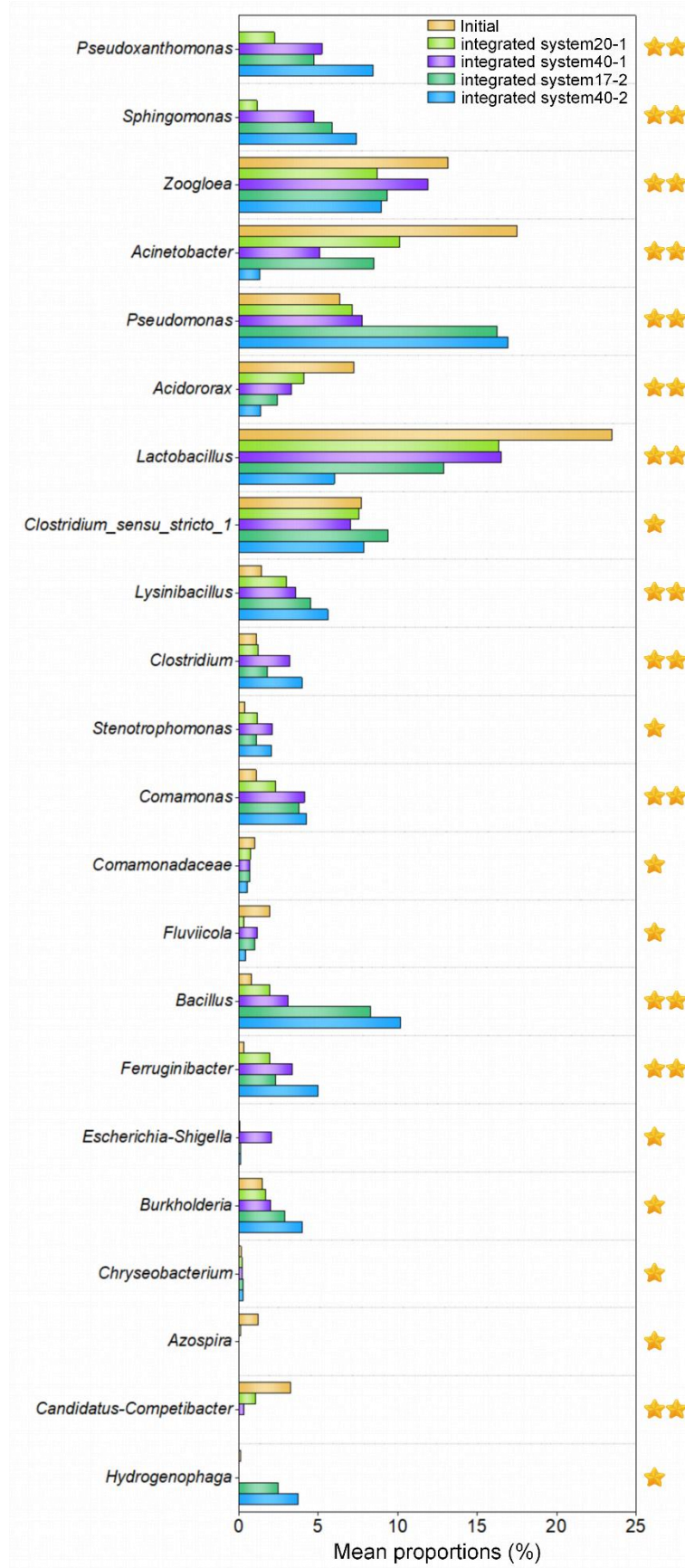
1212

Fig. S16. Mean proportions of microbial genus by Initial, integrated system20-1,

1214   integrated system40-1, integrated system17-2 and integrated system40-2 samples.

1215   Fig. S16 shows the bacteria genera with significant differences in Initial, integrated

1216   system20-1, integrated system40-1, integrated system17-2 and integrated system40-2

1217   samples. Compared with integrated system20-1 and integrated system40-1 with NMF,

1218   the community structure of integrated system17-2 and integrated system40-2 samples

1219   is significantly different, resulting in an obvious difference. It can be concluded that

1220   the MF has an effect on the structural changes of the biological community in the

1221   integrated system-2 reactors.
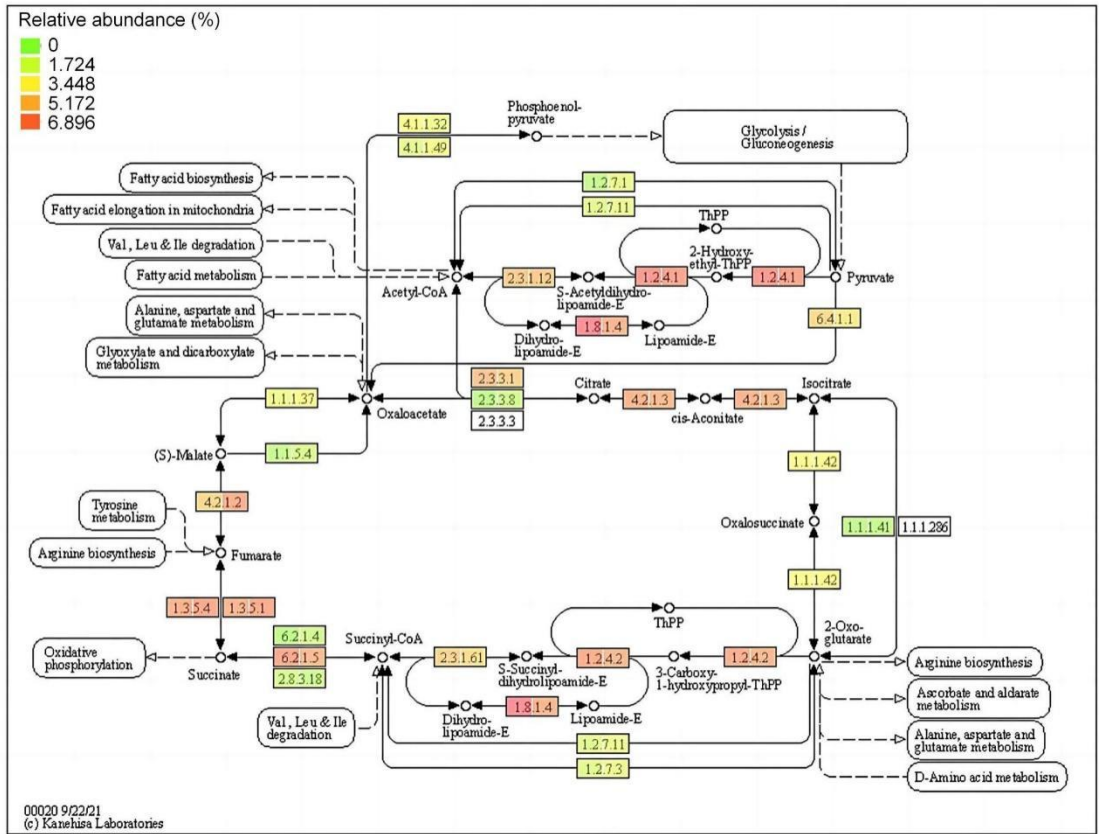
1222

1223

1224

1225

1226

1227

1228

1229

1230
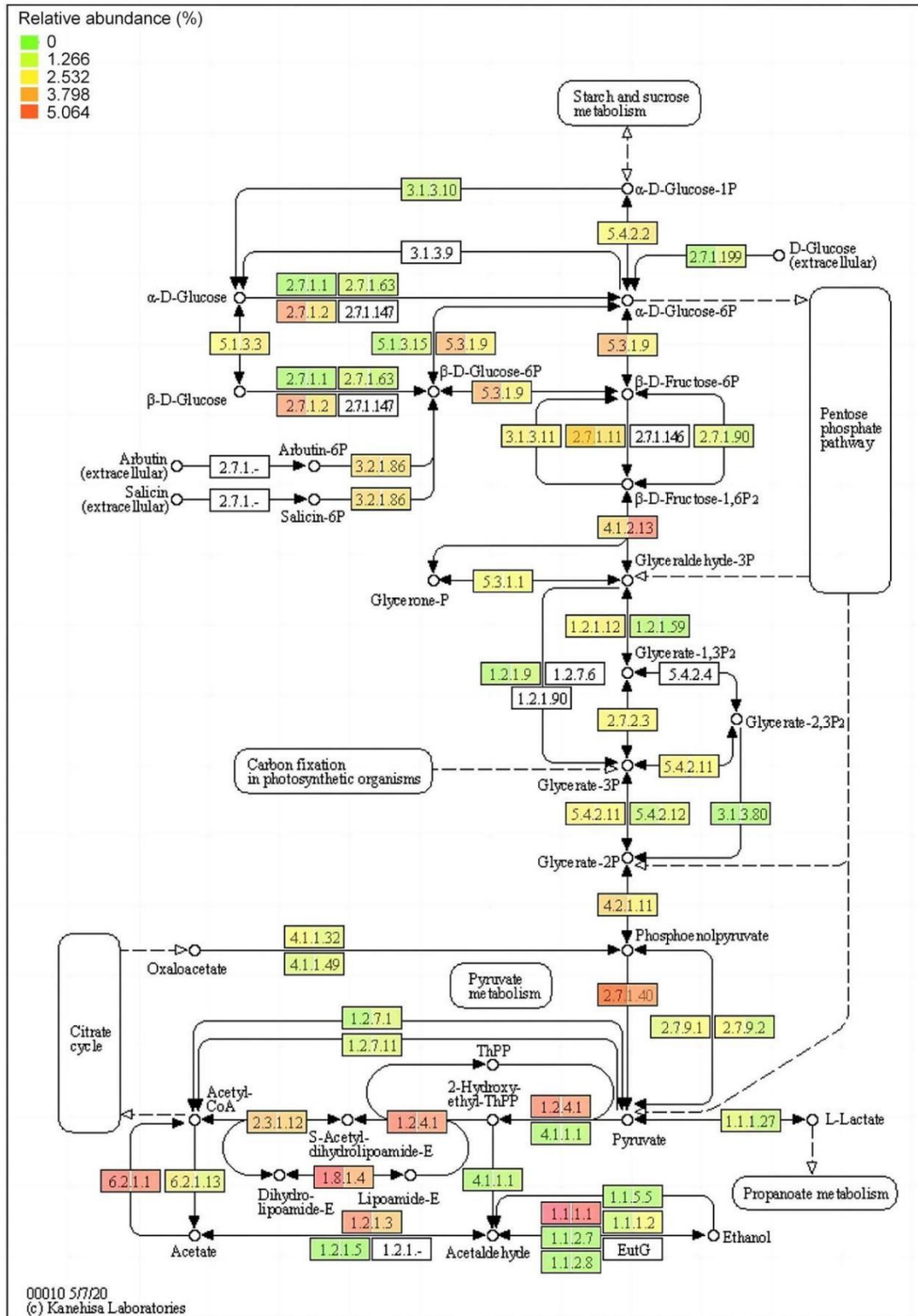
Fig. S17. Carbon metabolic pathways.

1231

1232

1233

1234

Fig. S18. TCA metabolic pathways.
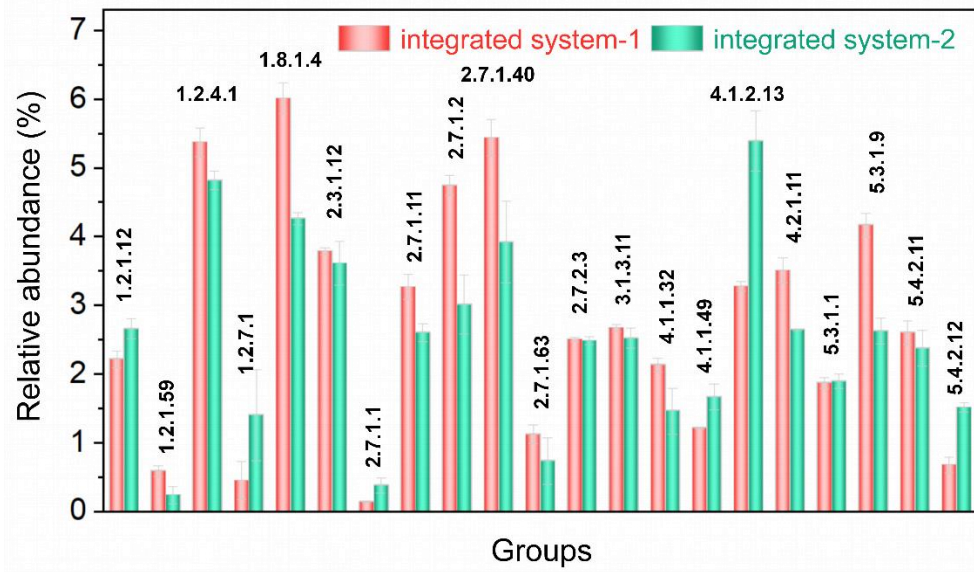
1242

Fig. S19. Map of differences in carbon metabolic pathways between integrated

system-1 and integrated system-2.
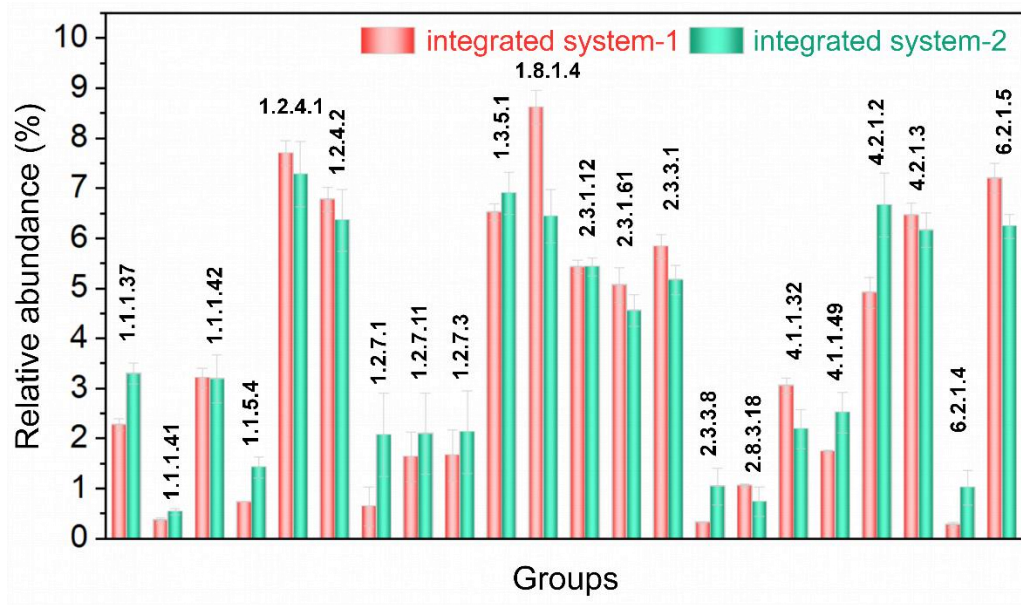
1243

1244

1245

1246

1247

1248

1249

1250

1251

1252

1253

1254

1255

1256

1257

Fig. S20. Map of differences in TCA metabolic pathways between integrated
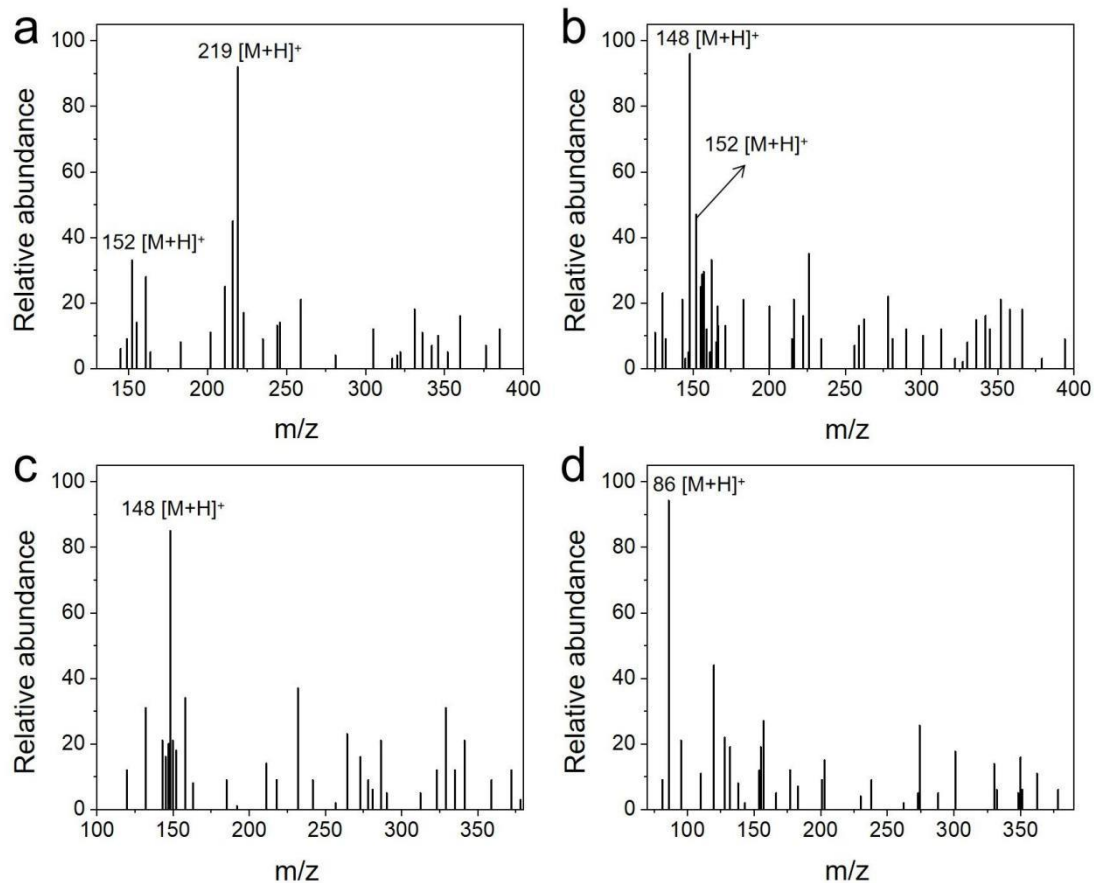
system-1 and integrated system-2.

1260

1261

1262

1263

1264

1265

1266

Fig. S21. Mass spectra of emerging intermediates when MF added in integrated

system-2 at different time.

Fig. S21 shows the MS spectra of the newly emerged intermediates of integrated

system-2 after applied MF. When the MF is applied, four new intermediates appear in

integrated system-2, whose M/Z are 219, 152, 148 and 86, respectively. The lower

molecular weight of intermediates detects in integrated system-2 compared with

integrated system-1 may be related to the enhancement of biodegradation within the

carrier in integrated system-2 by MF.

References

Gogate, P. R., Pandit, A. B., 1999. Survey of measurement techniques for gas-liquid mass transfer coefficient in bioreactors. Biochem. Eng. J. 4, 7-15.

Kumar, A., Gogate, P. R., Pandit, A. B., Wilhelm, A. M., Delmas, H., 2005. Investigation of induction of air due to ultrasound source in the sonochemical reactors. Ultrason. Sonochem. 12, 463-460.

Li, J., Cai, L., Shang, J., Yu, Y., Zhang, L., 2016. Giant enhancement of internal electric field boosting bulk charge separation for photocatalysis. Adv. Mater. 28, 4059-4064.

Yang, W., Zhang, L., Xie, J., Zhang, X., Liu, Q., Yao, T., Wei, S., Zhang, Q., Xie, Y., 2016. Enhanced photoexcited carrier separation in oxygen-doped $ZnIn_2S_4$ nanosheets for hydrogen evolution. Angew. Chem. Int. Ed. 55, 6716-6720.

Yu, C., He, H., Fan, Q., Xie, W., Liu, Z., Ji, H., 2019. Novel B-doped BiOCl nanosheets with exposed (001) facets and photocatalytic mechanism of enhanced degradation efficiency for organic pollutants. Sci. Total. Environ. 694, 133727.